

CENIC: Convex Error-controlled Numerical Integration for Contact

Vince Kurtz and Alejandro Castro

Abstract—State-of-the-art robotics simulators operate in discrete time. This requires users to choose a time step, which is both critical and challenging: large steps can produce non-physical artifacts, while small steps force the simulation to run slowly. Continuous-time error-controlled integration avoids such issues by automatically adjusting the time step to achieve a desired accuracy. But existing error-controlled integrators struggle with the stiff dynamics of contact, and cannot meet the speed and scalability requirements of modern robotics workflows. We introduce CENIC, a new continuous-time integrator that brings together recent advances in convex time-stepping and error-controlled integration, inheriting benefits from both continuous integration and discrete time-stepping. CENIC runs at fast real-time rates comparable to discrete-time robotics simulators like MuJoCo, Drake and Isaac Sim, while also providing guarantees on accuracy and convergence.

Index Terms—Simulation and Animation, Contact Modeling, Dexterous Manipulation, Dynamics.

I. INTRODUCTION

Simulation for contact-rich robotics has advanced significantly in recent years, driven by demands in policy learning, data generation, and model-based control. These efforts have led to highly optimized simulators that prioritize throughput, with implementations targeting modern CPU and GPU architectures. Most of these simulators—including Bullet [1], MuJoCo [2], Isaac Sim [3], RaiSim [4], Genesis [5], and Drake [6]—rely on discrete time-stepping with constraint-based contact formulations, a paradigm originally developed for computer graphics and game physics, where speed is favored over accuracy.

A central limitation of discrete time-stepping lies in time step selection. The appropriate time step depends on numerous factors, including object sizes, contact stiffnesses, control frequencies, and geometric resolution. In dexterous manipulation scenarios like that shown in Fig. 1, large robotic arms interacting with thin or stiff components introduce multiple time scales that are difficult to resolve uniformly. Small steps are often needed to avoid artifacts like interpenetration, tunneling, and impulse jitter. As simulation scenarios become more complex—modeling full factory floors or domestic environments—the number of contacts and degrees of freedom grows, making small time steps increasingly inefficient. Additionally, unexpected events like dropped objects or failed grasps can introduce unforeseen faster time scales, leading to nonphysical artifacts and undermining the predictive validity of the simulation.

In contrast, simulation tools in aerospace, automotive, and mechanical engineering have long prioritized accuracy, supported by formal frameworks for validation and verification (V&V) and uncertainty quantification (UQ) [7], [8]. Commercial multibody dynamics tools such as MSC Adams

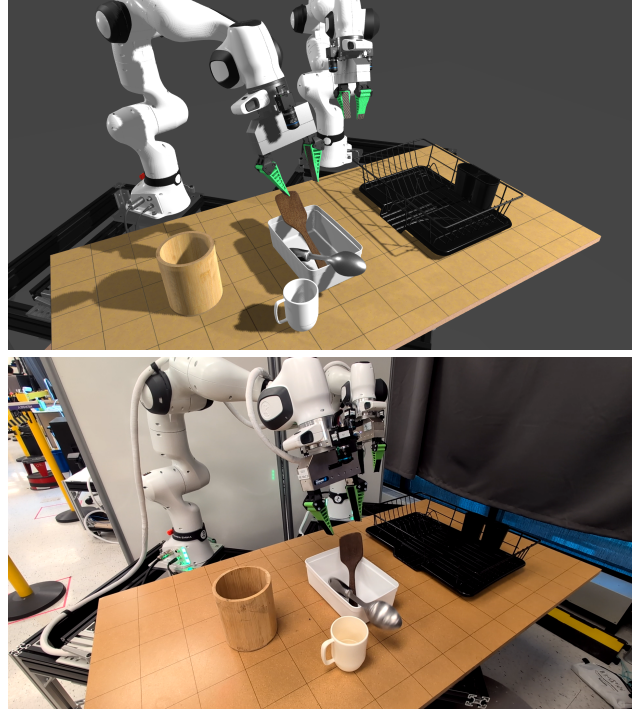


Fig. 1: A challenging bimanual manipulation scenario in simulation (top) and on hardware (bottom). A teleoperated robot drops several objects (spatula, spoon, mug) into a thin-walled bin. It then dumps the contents of the bin on a dish rack composed of thin wires. This scenario is particularly challenging: complex geometry, thin objects, heavy arms, and stiff joint controllers create a wide range of time scales that pose significant numerical difficulties. Discrete time-stepping methods struggle with passthrough, rattling, and unstable contact forces; CENIC eliminates these artifacts while completing the simulation at a real-time rate over 300%.

[9], Siemens Simcenter Motion [10], and RecurDyn [11] have been refined over decades and support integration with finite element analysis (FEA), hydraulic and electronic subsystem simulations [12], and computer aided design (CAD). These tools adopt a fundamentally different strategy: models of compliant contact with regularized friction allow all forces—including contact and friction—to be expressed as smooth functions of state. Importantly, these continuous models are grounded in experimentally validated contact mechanics, such as Hertz theory [13] for elastic forces and the Hunt & Crossley [14] model for dissipative effects. The resulting systems of ordinary differential equations (ODEs) are solved using error-controlled integration [15]. Such integrators adaptively adjust the time step to satisfy user-defined accuracy requirements. This decouples numerical error from modeling error—critical for certified engineering workflows.

But despite this reliability, engineering-level simulation tools are largely not suitable for robotics. Applications like manipulation and locomotion require high stiffnesses and

tight regularization of friction to approximate rigid contact. This leads to extremely stiff dynamics, where even state-of-the-art L -stable stiff integrators [15, §IV.3]—which effectively damp high-frequency modes—are forced to take prohibitively small steps, resulting in very slow simulations. Meanwhile, robotics applications like reinforcement learning, interactive teleoperation, and model predictive control require simulation speeds at (or well above) real time rates.

A. Contributions

We introduce CENIC, the first error-controlled integrator for contact-rich multibody dynamics tailored to robotics. CENIC builds on recent advances in convex-optimization-based time-stepping [16], [17] to produce a convex error-controlled integration scheme that automatically adjusts the time step to meet a user-specified accuracy. Unlike fixed-step schemes, CENIC evolves the simulated system in continuous time, mirroring the behavior of the physical world.

CENIC combines well-established error control strategies [15] with recently-developed irrotational contact field (ICF) theory [17]. As a result, CENIC blends the performance of discrete time-stepping with the mathematical rigor of error-controlled integration. This offers several benefits:

- 1) **Accuracy:** Users specify a desired accuracy (e.g., the number of significant digits in the solution) rather than a fixed time step. CENIC automatically adjusts the step size to meet this accuracy requirement.
- 2) **Consistency:** As accuracy is tightened, the numerical solution converges to the true continuous-time trajectory, avoiding artifacts such as the “gliding” characteristic of convex formulations, or the contact impulse “jitter” often seen in discrete time-stepping.
- 3) **Validated contact models.** CENIC is built on engineering-grade continuous-time contact models.
- 4) **Friction.** Unlike the discrete-time schemes typically used in robotics, CENIC can rigorously model both static and dynamic friction regimes.
- 5) **Modularity:** Arbitrary controllers and external systems are embedded in the convex formulation, enabling stable simulation of complex user-defined components.
- 6) **Convergence Guarantees:** Because the underlying time-stepping problem is convex, CENIC provides convergence guarantees independent of the current time step. This enables large steps even through complex contact transitions, where standard implicit integrators often fail or require many small steps.
- 7) **Efficiency:** CENIC outperforms traditional error-controlled integrators by orders of magnitude. While error-estimation introduces some overhead, overall simulation times can be faster than discrete-time methods, thanks to the ability to take small steps only when necessary. We also demonstrate practical techniques—such as selective Hessian reuse and adaptive convergence tolerances—to further improve speed.

CENIC provides a new foundation for scalable, physically consistent simulation in robotics, capable of handling large-

scale, contact-rich environments with provable guarantees on accuracy and convergence—ultimately enabling tighter sim-to-real alignment for manipulation, locomotion, reinforcement learning, and control applications.

B. Organization

Section II reviews background and related work on robotics simulation and error-controlled integration. Section III introduces our continuous-time modeling approach. We revisit ICF in Section IV, highlighting its role as a foundation for CENIC. Section V presents the proposed CENIC integrator, followed by performance optimizations (Section VI), experimental results (Section VII), discussion (Section VIII) and conclusions (Section IX).

II. BACKGROUND

Here we introduce notation (II-A) and review contact models (II-B). We then note that simulation approaches can be broadly classified into continuous-time (II-C) and discrete-time (II-D) formulations. The latter includes convex approximations (II-E), which offer tractable formulations with strong theoretical guarantees.

A. Multibody Dynamics

We consider articulated rigid-body systems described by joint coordinates. The state $\mathbf{x} = [\mathbf{q}; \mathbf{v}]$ collects generalized positions $\mathbf{q} \in \mathbb{R}^{n_q}$ and velocities $\mathbf{v} \in \mathbb{R}^{n_v}$, which are related kinematically by $\dot{\mathbf{q}} = \mathbf{N}(\mathbf{q})\mathbf{v}$. The dynamics under holonomic constraints are given by

$$\mathbf{M}(\mathbf{q})\dot{\mathbf{v}} + \mathbf{k}(\mathbf{q}, \mathbf{v}) = \boldsymbol{\tau} + \mathbf{J}(\mathbf{q})^T \mathbf{f} + \mathbf{G}(\mathbf{q})^T \boldsymbol{\lambda}, \quad (1a)$$

$$\text{s.t. } \mathbf{c}(\mathbf{q}) = \mathbf{0}, \quad (1b)$$

where $\mathbf{M}(\mathbf{q})$ is the mass matrix and $\mathbf{k}(\mathbf{q}, \mathbf{v})$ collects Coriolis and gravitational terms. Lagrange multipliers $\boldsymbol{\lambda}$ enforce holonomic constraints $\mathbf{c}(\mathbf{q}) = \mathbf{0}$, with $\mathbf{G}(\mathbf{q}) = \partial_{\mathbf{q}} \mathbf{cN}(\mathbf{q})$. Non-holonomic constraints can be treated analogously, but since their main use case—rolling—is already captured by our contact model, we focus on holonomic constraints for clarity. External forces, including actuation, are grouped in $\boldsymbol{\tau}$ and padded with zeros for unactuated degrees of freedom. The block rows $\mathbf{J}_i(\mathbf{q}) \in \mathbb{R}^{3 \times n_v}$ of the contact Jacobian define the relative contact velocities $\mathbf{v}_{c,i} = \mathbf{J}_i(\mathbf{q})\mathbf{v}$ at each contact. With contact normal $\hat{\mathbf{n}}_i$, we define normal $v_{n,i} = \mathbf{v}_{c,i} \cdot \hat{\mathbf{n}}_i$ and tangential $\mathbf{v}_{t,i} = \mathbf{v}_{c,i} - v_{n,i}\hat{\mathbf{n}}_i$ velocities. Contact forces \mathbf{f}_i are concatenated as $\mathbf{f} = [\mathbf{f}_0; \mathbf{f}_1; \dots]$.

B. Contact Modeling

When two solids make contact, they deform—at least microscopically—to prevent interpenetration. These deformations generate stresses. Contact forces are the integrated result of these stresses over the contact surface.

Compliant contact models forces as state-dependent algebraic functions of state, capturing quasistatic effects without solving the full elasticity problem. Compliant contact modeling dates back to the foundational work of Hertz [13],

[18], describing elastic contact under small strains. Hertz models are used in *point contact* approximations, which neglect the contact patch size. Later extensions incorporate local geometry and volume estimates [19], [20].

When the contact patch size cannot be neglected, the elastic foundation model (EFM) [13] offers a computationally efficient approximation. EFM has been applied to meshed geometries in [21], [22], and further refined in [23], [24] to provide smooth, differentiable forces with coarse meshes. Dissipative effects can be incorporated, most commonly using the Hunt & Crossley [14] model or similar variants.

Importantly, many of these compliant contact models have extensive experimental validation, and are thus widely used in commercial multibody simulation tools designed for certified engineering workflows [9]–[11]. However, for hard materials such as metals or ceramics, the resulting dynamics become numerically stiff and difficult to simulate.

Rigid contact is a popular alternative to stiff compliant contact, and idealizes bodies as infinitely stiff. This approximation underlies many real-time physics and gaming engines and is discussed further in Section II-D.

Friction arises from complex surface interactions at the microscale, including deformation of asperities and atomic adhesion. The Coulomb friction model provides a simple and widely-used approximation of the resulting net effects.

When contact surfaces do not slip, the Coulomb model specifies that friction forces satisfy $\|\mathbf{f}_t\| \leq \mu_s f_n$, where f_n is the normal force, \mathbf{f}_t is the tangential component of the friction force, and μ_s is the *coefficient of static friction*. During slip, the maximum dissipation principle (MDP) specifies that friction opposes the direction of slip

$$\mathbf{f}_t = -\mu_d \frac{\mathbf{v}_t}{\|\mathbf{v}_t\|} f_n,$$

where $\mu_d \leq \mu_s$ is the *coefficient of dynamic friction*.

Coulomb's friction law is discontinuous and multivalued. That is, in stiction, friction forces can have any magnitude between zero and $\mu_s f_n$. To avoid this, **regularized friction** models friction as a continuous function of slip velocity

$$\mathbf{f}_t = -\mu(\|\mathbf{v}_t\|) \frac{\mathbf{v}_t}{\|\mathbf{v}_t\|} f_n, \quad (2)$$

where $\mu(\cdot)$ smoothly transitions between the static and dynamic regimes (Fig. 2). For instance, Simbody [22] uses piecewise polynomials with C^2 -smooth transitions, with similar models in Adams [9] and RecurDyn [25].

C. Continuous-Time Contact Simulation

Together, compliant contact and regularized friction make the contact forces $\mathbf{f}_i(\mathbf{x})$ continuous functions of the state. In the absence of constraints, incorporating these forces into the dynamics (1) yields a system of ODEs. For clarity, we defer discussing constraints to Sec. III-D.

Continuous formulations offer several advantages for modeling contact dynamics: they handle both static and dynamic friction, build on contact models validated over decades

of experimentation, and can leverage error-controlled integration, which adaptively adjusts the time step to bound numerical deviations from true continuous solutions.

Error-controlled integration is a well-established topic, see [15] for an excellent reference. Given an ODE

$$\dot{\mathbf{x}} = \mathbf{f}(t, \mathbf{x}),$$

the integrator attempts a step of size δt from time t^n to $t^{n+1} = t^n + \delta t$, where superscripts index the step. Within this step, it computes two estimates of the next state, \mathbf{x}^{n+1} and $\hat{\mathbf{x}}^{n+1}$, and uses their difference to approximate the local truncation error

$$e^{n+1} = \|\mathbf{x}^{n+1} - \hat{\mathbf{x}}^{n+1}\| \approx \bar{c} \delta t^p, \quad (3)$$

where p is the order of the error estimate and \bar{c} a constant. For example, the Dormand-Prince integrator [26] computes \mathbf{x}^{n+1} with order 5 and $\hat{\mathbf{x}}^{n+1}$ with order 4, leading to a fifth order error estimate ($p = 5$). From $e^{n+1} = \bar{c} \delta t^p$ and $\varepsilon_{\text{acc}} = \bar{c} \delta t_{\text{new}}^p$, \bar{c} is eliminated to estimate a step size δt_{new} that attains a user-specified accuracy ε_{acc}

$$\delta t_{\text{new}} \leftarrow \delta t \left(\frac{\varepsilon_{\text{acc}}}{e^{n+1}} \right)^{1/p}. \quad (4)$$

If $e^{n+1} < \varepsilon_{\text{acc}}$, the step is accepted and the state is advanced to \mathbf{x}^{n+1} . Otherwise, the step is rejected, the time step is adjusted using (4), and the process is repeated until the estimated error falls below the specified accuracy.

Continuous formulations with error control are the foundation of most commercial multibody dynamics tools, including Adams [9], RecurDyn [11], Simcenter 3D [10], Simpack [27], and MotionSolve [28]. These tools are widely used in engineering, where predictive accuracy and fidelity are critical. Continuous simulation has also seen some success in biomechanics simulation, with the open-source Simbody [22] and commercial Hyfydy [29] as notable examples.

However, large mass ratios, stiff contact dynamics, and tightly regularized friction yield extremely stiff ODEs. As a result, even state-of-the-art L -stable integrators often struggle or stall on practical robotics problems.

D. Discrete-Time Contact Simulation

The stiffness of continuous-time dynamics makes accurate integration computationally demanding. Consequently, modern robotics and real-time simulators favor fixed-step discrete-time schemes, which forgo accuracy guarantees but maintain predictable computational costs.

Discrete-time formulations also permit the rigid-contact approximation, effectively modeling contact stiffness as infinite. Rigid contact with Coulomb friction can produce Painlevé paradoxes [30], where solutions may not exist. Theory resolves these paradoxes by allowing discrete velocity jumps and impulsive forces, formally casting the problem as a differential variational inequality (DVI) [31]. Thus discrete formulations integrate the dynamics (1) within the time interval $[t^n, t^{n+1})$ to derive a discrete momentum balance where impulses $\gamma_i = \int_{t^n}^{t^{n+1}} \mathbf{f}_i(t) dt$ replace contact forces \mathbf{f}_i and

discrete velocity changes replace continuous accelerations [32], [33]. Additional constraints enforce Coulomb’s law and the MDP, leading in general to a nonlinear complementarity problem (NCP) where velocities, impulses and constraint multipliers are the unknowns.

NCPs are NP-hard [34], and have proven extremely difficult to solve in practice. The literature on NCP-based simulation is vast, with techniques including linearized friction cones [33], [35], projected Gauss-Seidel (PGS) solvers [1], [4], [36], non-convex optimization [34], [37], non-smooth formulations [38], interior point methods [39], and alternating direction method of multipliers (ADMM) solvers [40].

Many of these approaches have demonstrated excellent performance in practice, at the expense of sacrificing accuracy and convergence guarantees. Though not widely accepted in robotics, commercial platforms such as Algoryx [41] and Vortex [42] also adopt discrete time-stepping methods for real-time multibody dynamics, targeting domains like virtual prototyping, operator training, and vehicle simulation.

E. Convex Approximations

Without existence and convergence guarantees, NCP-based simulations face robustness challenges. Techniques such as constraint relaxation and numerical stabilization (e.g. *constraint force mixing* [43]) can alleviate these challenges but introduce artificial compliance—the very phenomenon rigid NCP formulations were designed to avoid.

To avoid these issues, Anitescu introduced a *convex relaxation* of the contact problem [44]. Later, Todorov introduced a regularized convex formulation with a unique solution in MuJoCo [45], though at the expense of non-physical regularization parameters and noticeable constraint drift [46]. The implementation in MuJoCo is remarkably performant and thus widely used in the robotics and RL communities. Chrono [47], Siconos [48], and Drake [6] also implement convex time-stepping methods. The SAP [16] formulation in Drake leverages numerical regularizations that correspond to the physics of compliant contact.

However, all of these Anitescu-based convex relaxations suffer from common problems. They all exhibit *gliding* or *hydroplaning* artifacts, where sliding objects hover at a distance proportional to slip velocity. This gliding artifact was reported inadequate for quadruped simulation in [49]. Even more acute, for compliant formulations like those in MuJoCo [45] and SAP [16], gliding is also proportional to the dissipation parameter and does not vanish as the time step is reduced [17]. Thus users are forced to trade-off contact modeling accuracy with numerical artifacts, often simulating models that are further from reality to limit numerical issues.

Most recently, irrotational contact fields (ICF) theory [17] establishes conditions under which engineering-grade compliant contact models can be embedded in a convex formulation. Moreover, ICF introduces a *lagged* convex approximation that eliminates gliding artifacts. ICF regularizes friction

in terms of a single *stiction tolerance* velocity parameter v_s such that friction forces are given by

$$\mathbf{f}_t = -\mu_d \frac{\mathbf{v}_t}{\sqrt{\|\mathbf{v}_t\|^2 + v_s^2}} f_n, \quad (5)$$

with magnitude

$$\|\mathbf{f}_t\| = \mu_d f(\|\mathbf{v}_t\|/v_s) f_n.$$

Here $f(s) = s/\sqrt{s^2 + 1}$ a sigmoid function resulting from ICF’s convex potential. Sticking contact corresponds to $\|\mathbf{v}_t\| < v_s$, while slipping contacts with $\|\mathbf{v}_t\| > v_s$ satisfy Coulomb’s law and the MDP. ICF’s robustness and strong mathematical guarantees allow it to operate with extremely tight regularization ($v_s \approx 0.1$ mm/s), as required for demanding robotics applications like dexterous manipulation. As reference, the biomechanics simulator Simbody [22] uses a default stiction tolerance of 1 cm/s while Hyfydy [29] and MSC Adams [50, p. 145] use 10 cm/s.

III. CONTINUOUS-TIME DYNAMICS MODEL

CENIC takes a continuous-time approach (Section II-C). Here we detail our particular choices for modeling contact, friction, and external control systems in continuous time.

A. Compliant Contact

We build on the contact models implemented in Drake [17], [24]. These compliant models provide algebraic formulae to compute the elastic contribution to the normal contact force $f_{e,i}(\mathbf{q})$ at the i -th contact point as a function of configuration \mathbf{q} . For simplicity, in the following we drop the contact index i .

Point contact models the normal force as $f_e(\mathbf{q}) = k(-\phi(\mathbf{q}))_+$, where $\phi(\mathbf{q})$ is the signed distance between two interacting geometries (negative when geometries overlap), k is the stiffness, and $(a)_+ = \max(0, a)$.

Hydroelastic contact [23] models continuous contact patches, discretized into polygons [24] of area $A(\mathbf{q})$, with elastic normal force $f_e(\mathbf{q}) = A(\mathbf{q}) p_e(\mathbf{q})$, where $p_e(\mathbf{q})$ is the hydroelastic contact pressure at the polygon’s centroid [24]. In this model, stiffness is parameterized by a *hydroelastic modulus* (similar to, though not the same as, Young’s modulus for a given material).

For both point and hydroelastic models, we incorporate the Hunt & Crossley [14] model of dissipation to write the normal force as a function of the system state \mathbf{x}

$$f_n(\mathbf{x}) = f_e(\mathbf{q})(1 - d v_n(\mathbf{x}))_+, \quad (6)$$

where $v_n(\mathbf{x})$ is the normal velocity (positive when objects move apart) and d is the Hunt & Crossley dissipation parameter.

B. Regularized Friction

We design a regularized friction model that extends (5) to resolve both static and dynamic friction

$$\mathbf{f}_t = -\mu(\|\mathbf{v}_t\|/v_s) \frac{\mathbf{v}_t}{\sqrt{\|\mathbf{v}_t\|^2 + v_s^2}} f_n, \quad (7)$$

where the friction coefficient is given by

$$\mu(s) = (\mu_s - \mu_d)\sigma(s) + \mu_d, \quad (8)$$

with

$$\sigma(s) = \frac{1}{2} \left(1 - \frac{f(|s| - \Delta)}{f(\Delta)} \right),$$

conveniently defined in terms of the ICF's sigmoid function in (5). Δ measures the width of the transition region, as shown in Fig. 2. We found that CENIC works particularly well with $\Delta = 10$, while maintaining ICF's tight stiction modeling when $\|\mathbf{v}_t\| < v_s$.

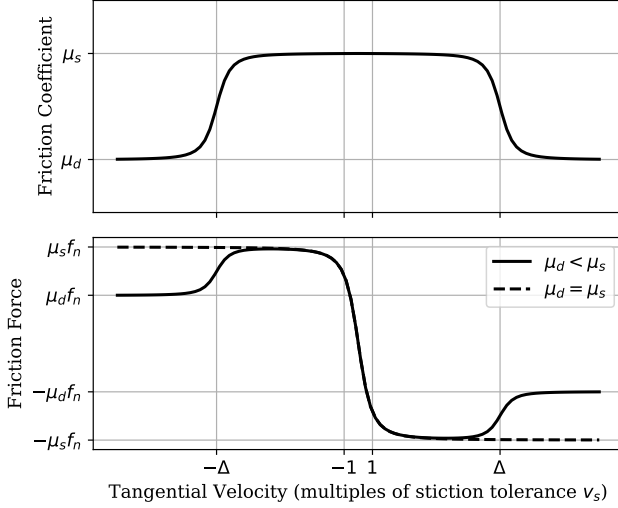


Fig. 2: CENIC's regularized friction model captures both static (μ_s) and dynamic (μ_d) friction regimes. Our default stiction tolerance is $v_s = 0.1$ mm/s, with a transition width of $\Delta = 10$.

C. External Systems

Useful robotics simulations involve not only multibody dynamics, but also external systems like controllers, sensors, planners, and learned policies. Such external systems can be described by a separate dynamical system in a feedback loop, as illustrated in Fig. 3.

The external system takes as input the multibody state \mathbf{x} and outputs actuator forces $\boldsymbol{\tau}$. These forces may depend on the external system's own state \mathbf{z} , which evolves with dynamics

$$\dot{\mathbf{z}} = \mathbf{h}(\mathbf{z}, \mathbf{x}), \quad (9a)$$

$$\boldsymbol{\tau} = \mathbf{g}(\mathbf{z}, \mathbf{x}). \quad (9b)$$

The external system is often composed of many interconnected sub-systems. In Drake, dynamical systems are modeled using *block diagrams* with *graph-based representations*,

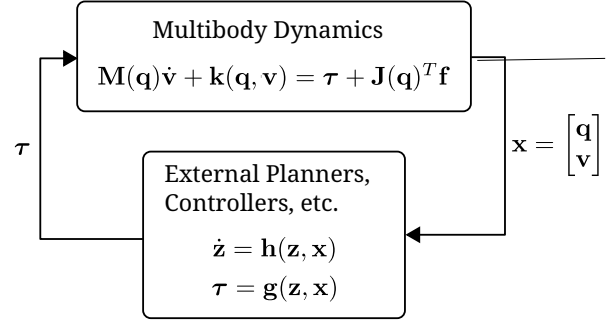


Fig. 3: In practice, robotics simulations involve multibody dynamics connected to controllers, planners, and other components. We abstract these elements as a single external dynamical system. Unlike discrete formulations, CENIC integrates external systems implicitly, an effective strategy even for stiff feedback dynamics.

where nodes (blocks) denote components such as integrators, gains, or state-space models, and directed edges (signals) define variable flow between them. MATLAB, SimuLink, and OpenModelica provide similar representations.

D. Full Dynamical System

The constrained multibody dynamics (1), combined with the compliant contact and regularized friction models introduced above, describe the dynamics of the multibody system. Together with the external system dynamics (9), the entire system evolves according to

$$\mathbf{M}(\mathbf{q})\dot{\mathbf{v}} + \mathbf{k}(\mathbf{q}, \mathbf{v}) = \mathbf{g}(\mathbf{z}, \mathbf{x}) + \mathbf{J}(\mathbf{q})^T \mathbf{f}(\mathbf{x}) + \mathbf{G}(\mathbf{q})^T \boldsymbol{\lambda}, \quad (10a)$$

$$\dot{\mathbf{q}} = \mathbf{N}(\mathbf{q})\mathbf{v}, \quad (10b)$$

$$\dot{\mathbf{z}} = \mathbf{h}(\mathbf{z}, \mathbf{x}), \quad (10c)$$

$$\text{s.t. } \mathbf{c}(\mathbf{q}) = \mathbf{0}. \quad (10d)$$

This index-3 system of differential-algebraic equations (DAEs) fully defines the *model*, encompassing both physics and external interactions. Its high index introduces challenges such as constraint drift and difficulty in finding consistent initial conditions. Moreover, (10) is highly stiff, and even state-of-the-art stiff integrators (Sec. VII) often struggle or fail to solve it. In the following sections, we show how CENIC brings together the best of convex time-stepping and error-controlled integration to efficiently solve this DAE.

IV. IRROTATIONAL CONTACT FIELDS

Given its central role in this work, this section briefly introduces ICF [17], related notation, and the properties that make ICF a key building block for CENIC. We refer the reader to [17] for further details and derivations.

ICF advances the multibody state ($\mathbf{x} = [\mathbf{q}; \mathbf{v}]$) with a first-order symplectic Euler scheme, where velocities \mathbf{v}^{n+1} are solved implicitly from the discrete momentum balance

$$\mathbf{M}^n(\mathbf{v}^{n+1} - \mathbf{v}^n) + \delta t \mathbf{k}^n = \mathbf{J}^{nT} \boldsymbol{\gamma}(\mathbf{v}^{n+1}; \mathbf{x}^n, \delta t), \quad (11)$$

and then used to update configurations

$$\mathbf{q}^{n+1} = \mathbf{q}^n + \delta t \mathbf{N}^n \mathbf{v}^{n+1}. \quad (12)$$

The mass matrix ($\mathbf{M}^n = \mathbf{M}(\mathbf{q}^n)$), Coriolis and potential terms ($\mathbf{k}^n = \mathbf{k}(\mathbf{q}^n, \mathbf{v}^n)$), constraint Jacobian ($\mathbf{J}^n = \mathbf{J}(\mathbf{q}^n)$), and projection matrix ($\mathbf{N}^n = \mathbf{N}(\mathbf{q}^n)$) are approximated explicitly to first order, much like a first-order Implicit-Explicit (IMEX) scheme [51]. For simplicity, we defer discussion of constraints and actuation to Sections IV-D and IV-E.

The semicolon notation $\gamma(\mathbf{v}^{n+1}; \mathbf{x}^n, \delta t)$ denotes that impulses, though evaluated implicitly on \mathbf{v}^{n+1} , stem from an *incremental potential* $\ell(\mathbf{v}; \mathbf{x}^n, \delta t)$ built using the previous-step state \mathbf{x}^n . More precisely, $\gamma(\mathbf{v}^{n+1}; \mathbf{x}^n, \delta t)$ concatenates impulses γ_i^{n+1} from each constraints.

A. Compliance Approximation

ICF approximates normal impulses (6) to first-order, fully implicit in \mathbf{v}^{n+1} to ensure strong numerical stability. For normal contact velocity $v_{n,i}$, the corresponding impulse is

$$\gamma_{n,i}^{n+1}(v_{n,i}; \mathbf{x}^n, \delta t) = \delta t (f_{e,i}^n - \delta t k_i v_{n,i})_+ (1 - d_i v_{n,i})_+, \quad (13)$$

where $f_{e,i}^n = f_{e,i}(\mathbf{q}^n)$ is the elastic contribution given algebraically by the compliant contact model (6), k_i is the contact stiffness and d_i the Hunt & Crossley dissipation. For point contact, stiffness is a user supplied parameter. For hydroelastic contact, the stiffness combines cell area and hydroelastic pressure gradient [24].

B. Friction Approximation

ICF theory describes a family of convex contact approximations. *SAP*, *Lagged* and *Similar* are solutions to ICF that belong to this family [17]. CENIC builds on the *Lagged* approach, which approximates the tangential component of the impulse to first order as

$$\gamma_{t,i}^{n+1} = -\mu_{d,i} \frac{\mathbf{v}_{t,i}^{n+1}}{\sqrt{\|\mathbf{v}_{t,i}^{n+1}\|^2 + v_s^2}} \gamma_{n,i}^n. \quad (14)$$

Note that the tangential component is implicit in the velocities, while the normal component is *lagged*, with $\gamma_{n,i}^n = \delta t f_{n,i}(\mathbf{x}^n)$ from (6).

C. Convex Formulation

ICF shows we can solve an unconstrained convex optimization problem for velocities at the next time step

$$\mathbf{v}^{n+1} = \arg \min_{\mathbf{v}} \ell(\mathbf{v}; \mathbf{x}^n, \delta t), \quad (15)$$

where optimality condition $\nabla \ell = 0$ corresponds to the discrete momentum balance (11), together with the first-order approximations (13) and (14).

The cost can be written as

$$\ell(\mathbf{v}; \mathbf{x}^n, \delta t) = \frac{1}{2} \mathbf{v}^T \mathbf{A} \mathbf{v} - \mathbf{r}^T \mathbf{v} + \ell_c(\mathbf{v}; \mathbf{x}^n, \delta t), \quad (16)$$

where $\mathbf{A} = \mathbf{M}^n$, $\mathbf{r} = \mathbf{M}^n \mathbf{v}^n - \delta t \mathbf{k}^n$, and $\ell_c = \sum_i \ell_i$ is separable into individual potentials ℓ_i for each constraint. The gradient of the constraint potential satisfies

$$\nabla \ell_c(\mathbf{v}; \mathbf{x}^n, \delta t) = -\mathbf{J}^{nT} \boldsymbol{\gamma}(\mathbf{v}; \mathbf{x}^n, \delta t). \quad (17)$$

In addition to contact, constraints such as couplers, distance constraints, limits, and welds can be included in this formulation, as described below.

D. Limit and Holonomic Constraints

ICF can incorporate holonomic constraints (1b) and limit constraints, which we express in the general form

$$c_{l,i} \leq c_i(\mathbf{q}) \leq c_{u,i},$$

for the i -th constraint, with $c_{l,i}$ and $c_{u,i}$ the lower and upper bounds. The holonomic case corresponds to $c_{l,i} = c_{u,i}$.

Limit constraints admit impacts with discontinuous velocity jumps and thus must be treated within the context of DVIs, where complementarity conditions between constraints and their multipliers are enforced. ICF avoids the complementarity formulation by instead using a regularized (compliant) model

$$\begin{aligned} \lambda_{l,i} &= k_i (c_{l,i} - c_i - \tau_i \dot{c}_i)_+ H(c_{l,i} - c_i), \\ \lambda_{u,i} &= -k_i (c_i - c_{u,i} + \tau_i \dot{c}_i)_+ H(c_i - c_{u,i}), \end{aligned}$$

where the Heaviside function $H(x)$ is necessary to avoid action at a distance. Stiffness and Kelvin–Voigt damping are set according to the *near-rigid* estimation [16]

$$k_i = \frac{1}{4\pi^2 \beta^2} \frac{m_i}{\delta t^2}, \quad \tau_i = \frac{\beta}{\pi} \delta t, \quad (18)$$

with $m_i = \|\mathbf{W}_{ii}\|^{-1}$, and \mathbf{W}_{ii} is a diagonal estimate of the Delassus operator $\mathbf{W} = \mathbf{G}\mathbf{M}\mathbf{G}^T$ [16]. In this *near-rigid* regime, the i -th constraint behaves as a critically damped harmonic oscillator with period $\beta \delta t$. A value $\beta = 0.1$ is typical and delivers a tight constraint enforcement in practice.

ICF uses a first-order Taylor expansion

$$\begin{aligned} c_i^{n+1} &= c_i^n + \delta t \dot{c}_i^{n+1}, \\ \dot{c}_i^{n+1} &= \mathbf{G}_i^n \mathbf{v}^{n+1}, \end{aligned}$$

with $c_i^n = c_i(\mathbf{q}^n)$ and $\mathbf{G}_i = \partial_{\mathbf{q}} c_i \mathbf{N}(\mathbf{q})$ the i -th row of $\mathbf{G}(\mathbf{q})$ in (10a), to approximate limit constraint forces as

$$\begin{aligned} \lambda_{l,i} &= k_i (\delta t + \tau_i) (\hat{v}_{l,i} - \dot{c}_i^{n+1})_+, & \hat{v}_{l,i} &= \frac{c_{l,i} - c_i^n}{\delta t + \tau_i}, \\ \lambda_{u,i} &= -k_i (\delta t + \tau_i) (\dot{c}_i^{n+1} - \hat{v}_{u,i})_+, & \hat{v}_{u,i} &= \frac{c_{u,i} - c_i^n}{\delta t + \tau_i}. \end{aligned}$$

Note that the Heaviside term was neglected, allowing *action-at-a-distance* $\tau_i \dot{c}_i^{n+1} = \beta/\pi \delta t \dot{c}_i^{n+1}$. This $\mathcal{O}(\delta t)$ term goes to zero as the time step is decreased.

Finally, the regularized approximation contributes to (15) via the cost functions

$$\begin{aligned} \ell_{l,i}(\dot{c}) &= \frac{1}{2} \delta t (\delta t + \tau_i) k_i (\dot{c} - \hat{v}_{l,i})_+^2, \\ \ell_{u,i}(\dot{c}) &= \frac{1}{2} \delta t (\delta t + \tau_i) k_i (\hat{v}_{u,i} - \dot{c})_+^2. \end{aligned}$$

Since stiffness is proportional to δt^{-2} in (18), the rigid approximation is tightened as the time step is reduced.

E. Linear Control Laws with Effort Limits

Linear effort-limited control laws can also be embedded in the convex ICF formulation. In Sec. V-C below, we will leverage this property to handle arbitrary external systems.

In particular, we consider control laws of the form

$$\begin{aligned} \mathbf{y} &= -\mathbf{C}\mathbf{v} + \mathbf{b} \\ \boldsymbol{\tau} &= \text{clamp}(\mathbf{y}; \mathbf{e}) \end{aligned} \quad (19)$$

where matrix \mathbf{C} is positive diagonal, and \mathbf{b} is a bias term. The clamp function is defined componentwise, i.e. $\text{clamp}(\mathbf{x}; \mathbf{e})_i = \max(-e_i, \min(e_i, x_i))$.

For such controllers, we can write the convex potential

$$\begin{aligned} \ell_{e,i}(v_i) &= \delta t \begin{cases} -e_i v_i & \text{if } y_i \geq e_i, \\ e_i v_i & \text{if } y_i \leq -e_i, \\ \frac{1}{2c_i}(-c_i v_i + b_i)^2 & \text{if } y_i \in (-e_i, e_i). \end{cases} \\ \ell_e(\mathbf{v}) &= \sum_i \ell_{e,i}(v_i), \end{aligned} \quad (20)$$

such that $-\nabla \ell_e$ recovers (19). ICF's curl condition $\partial \gamma_i / \partial v_j = \partial \gamma_j / \partial v_i$ on the control law (19) leads to the requirement that \mathbf{C} must be positive diagonal.

F. Consistency

In total, the symplectic IMEX scheme (11)-(12) is first order, with first order approximations of compliance (13) and friction (14). Most importantly, this scheme is *consistent* with the continuous model described in Sec. III-D. In other words, the discrete scheme recovers exact trajectories of the DAE (10) in the limit of vanishing step size, $\delta t \rightarrow 0$. This consistency property is essential for error-controlled integration, and allows ICF to form the core building block upon which we develop CENIC.

V. CONVEX ERROR-CONTROLLED INTEGRATION

Even advanced L -stable integrators frequently fail to advance the DAE system (10), particularly for stiff (near-rigid) materials and the tight friction regularization ($v_s \approx 0.1$ mm) required for robot manipulation. Numerical experiments demonstrate this in Section VII. We identify three main factors underlying the difficulties of conventional integrators. These motivate the design of CENIC, which addresses these challenges to deliver greater robustness, accuracy, and speed:

- 1) **Newton convergence.** Newton–Raphson iterations in implicit schemes often diverge, forcing the integrator to reject steps and discard work. By building on the convexity of ICF, CENIC guarantees convergence for any δt , eliminating discarded iterations.
- 2) **Friction instabilities.** Friction is tightly coupled to tangential velocities (7). Therefore, to maintain stable friction, conventional integrators must monitor velocities, which in turn requires small time steps to resolve impact transitions (see Fig. 4). In contrast, ICF yields well-converged tangential velocities and coherent friction forces at any time step, allowing CENIC to rely

on position error as a robust accuracy metric and to take larger time steps (Section V-E).

- 3) **Expensive geometry updates.** Standard implicit integrators—and some discrete solvers [37]—require costly geometry queries at each Newton iteration. ICF's Taylor expansion (13) implicitly couples forces without repeated queries, so CENIC needs only two geometry evaluations per step.

Moreover, for limit and holonomic constraints, CENIC regularizes the original DAE (10) using ICF in a way similar to a Singular Perturbation Problem (SPP) [15, §VI], producing trajectories that quickly settle onto the constraint manifold. The rapid $\mathcal{O}(\beta \delta t)$ transient compensates for the missing freedom in choosing consistent initial conditions in the DAE [15, §VI.3], while error control ensures that the influence of this transient is bounded by the desired accuracy. Furthermore, as the user-specified accuracy tightens and time steps shrink, ICF's near-rigid regularization, which scales as δt^{-2} (18), yields increasingly tight constraint enforcement.

Next we detail how CENIC leverages ICF to compute both a propagated solution and a local error estimate. We present two strategies: a first-order scheme in Section V-A and a second-order scheme in Section V-B.

A. First-Order Step-Doubling Method

To ease notation, we denote the full state update (11)-(12) from state $\mathbf{x}^n = [\mathbf{q}^n; \mathbf{v}^n]$ at time t^n to state $\mathbf{x}^{n+1} = [\mathbf{q}^{n+1}; \mathbf{v}^{n+1}]$ at time $t^{n+1} = t^n + \delta t$ as

$$\mathbf{x}^{n+1} = \text{ICF}(\mathbf{x}^n; \delta t). \quad (21)$$

With step-doubling, we compute the propagated solution by taking two successive steps of size $\delta t/2$

$$\mathbf{x}^{n+1/2} = \text{ICF}(\mathbf{x}^n; \delta t/2), \quad (22)$$

$$\mathbf{x}^{n+1} = \text{ICF}(\mathbf{x}^{n+1/2}; \delta t/2), \quad (23)$$

and compare against a full-step

$$\hat{\mathbf{x}}^{n+1} = \text{ICF}(\mathbf{x}^n; \delta t). \quad (24)$$

While this requires three convex solves per step, each solve is closely related to the others, and can be effectively warm-started (Sec. VI-A). Moreover, quantities to build the full-step problem are the same as those for the first half-step, and can be reused. Thus only two geometry queries are required, since both (22) and (24) use the same geometric information at \mathbf{x}^n , while (23) requires a separate query at $\mathbf{x}^{n+1/2}$.

Because ICF is first order, the resulting error estimate $e^{n+1} = \|\mathbf{x}^{n+1} - \hat{\mathbf{x}}^{n+1}\|$ is second order [15, §II.4]: overall, we obtain a first-order integration scheme with a second-order error estimate.

B. Second-Order Trapezoid Method

As above, we compute a full step $\hat{\mathbf{x}}^{n+1}$ from (24). From this implicit solution, we define *bar* quantities that approximate terms evaluated at $t^{n+1/2} = t^n + \delta t/2$

$$\begin{aligned}\bar{\mathbf{M}} &= (\mathbf{M}(\hat{\mathbf{q}}^{n+1}) + \mathbf{M}(\mathbf{q}^n))/2, \\ \bar{\mathbf{k}} &= (\mathbf{k}(\hat{\mathbf{q}}^{n+1}) + \mathbf{k}(\mathbf{q}^n))/2, \\ \bar{\mathbf{N}} &= (\mathbf{N}(\hat{\mathbf{q}}^{n+1}) + \mathbf{N}(\mathbf{q}^n))/2,\end{aligned}$$

and write our second-order scheme as

$$\bar{\mathbf{M}}(\mathbf{v}^{n+1} - \mathbf{v}^n) + \delta t \bar{\mathbf{k}} = \overline{\mathbf{J}^T \boldsymbol{\gamma}}, \quad (25a)$$

$$\mathbf{q}^{n+1} = \mathbf{q}^n + \frac{\delta t}{2} \bar{\mathbf{N}}(\mathbf{v}^{n+1} + \mathbf{v}^n). \quad (25b)$$

Without contact ($\overline{\mathbf{J}^T \boldsymbol{\gamma}} = 0$), (25) corresponds to a second-order explicit trapezoid rule. With contact, the key is to obtain a second-order approximation of the contact contribution $\overline{\mathbf{J}^T \boldsymbol{\gamma}}$. For stability, we seek an implicit approximation in \mathbf{v}^{n+1} . To that end, we propose a scheme based on the implicit trapezoid method

$$\begin{aligned}\overline{\mathbf{J}^T \boldsymbol{\gamma}} &\stackrel{\text{def}}{=} \frac{1}{2} \left(\mathbf{J}^{nT} \boldsymbol{\gamma}^n + \mathbf{J}^{n+1T} \boldsymbol{\gamma}^{n+1} \right) \\ &\approx \frac{1}{2} \left(\mathbf{j}^n + \hat{\mathbf{J}}^T \boldsymbol{\gamma}^{n+1} \right),\end{aligned}$$

where $\mathbf{j}^n = \mathbf{J}^{nT} \boldsymbol{\gamma}^n$ are the generalized impulses at the previous time step and *hat* quantities are next time step estimates from $\hat{\mathbf{x}}^{n+1}$. We treat the Jacobian explicitly, $\hat{\mathbf{J}} = \mathbf{J}(\hat{\mathbf{q}}^{n+1})$, reusing values from the initial full step. We treat the impulses implicitly, setting up an incremental potential to compute $\boldsymbol{\gamma}^{n+1} = \boldsymbol{\gamma}(\mathbf{v}^{n+1}; \hat{\mathbf{x}}^{n+1}, \delta t)$.

Unlike (17), this incremental potential uses the state at t^{n+1} rather than at t^n . Therefore we must introduce approximations implicit in \mathbf{v}^{n+1} that can use $\hat{\mathbf{x}}^{n+1}$. We define

$$\hat{f}_{e,i}^n = f_{e,i}(\hat{\mathbf{q}}^{n+1}) + \delta t k_i \hat{v}_{n,i}$$

to be used in (13), where $\hat{v}_{n,i}$ is the normal component of $\hat{\mathbf{v}}_{c,i} = \hat{\mathbf{J}}_i \hat{\mathbf{v}}^{n+1}$. That is, $\hat{f}_{e,i}^n$ is a first-order estimation of the elastic normal force *stepped backwards* from $\hat{\mathbf{q}}^{n+1}$.

Comparing our second-order scheme with (11), we notice that it corresponds to an ICF problem (16) with

$$\begin{aligned}\mathbf{A} &= \bar{\mathbf{M}}, \\ \mathbf{r} &= \bar{\mathbf{M}} \mathbf{v}^n - \delta t \bar{\mathbf{k}} + \frac{1}{2} \mathbf{j}^n, \\ \mathbf{J} &= \frac{1}{2} \hat{\mathbf{J}},\end{aligned}$$

and an incremental approximation for $\boldsymbol{\gamma}^{n+1}$ from $\hat{f}_{e,i}^n$. We solve this ICF problem for \mathbf{v}^{n+1} and update configurations with (25b) to achieve second-order accuracy.

Finally, we compare the second-order \mathbf{x}^{n+1} with the first-order $\hat{\mathbf{x}}^{n+1}$ to obtain a second-order error estimate. In total, this second-order trapezoid method requires only two convex ICF solves and two geometry queries at each step: one at \mathbf{x}^n to build the first-order update and one at $\hat{\mathbf{x}}^{n+1}$ to build the second-order update. As we will show in Sec. VII-A, this second-order method improves energy conservation, but

at the expense of losing desirable stability properties (in particular, the implicit trapezoid rule is not L -stable).

C. External Systems

Stiff external systems, such as a high-gain PID controller, can force error-controlled integration to take many small time steps, slowing simulation speeds. A more complex example is the vacuum gripper in Section VII-D1, where vacuum forces increase rapidly as function of distance to the suction caps, thus leading to stiff dynamics and short time scales.

To handle such cases, which are common in robotics, this section develops an implicit scheme for integrating external dynamical systems tightly coupled to the multibody dynamics. The resulting scheme can be applied to arbitrary external systems, enabling the stable treatment of complex controllers and user-defined force elements.

The key idea is to use first-order approximations of the external system dynamics (9) to express actuation inputs $\boldsymbol{\tau}^{n+1}$ as an implicit function of \mathbf{v}^{n+1} in the linear form (19), compatible with ICF.

Remark 1. *Similarly, we could use second-order approximations of the external system dynamics compatible with our second-order ICF. However, as we will show in Section VII, the step-doubling strategy is much more effective in practice and thus we present only the first-order approximation here.*

First, we use (12) to write a first-order approximation about \mathbf{q}^n that eliminates configurations from (9)

$$\dot{\mathbf{z}}(\mathbf{z}, \mathbf{v}) \approx \mathbf{h}(\mathbf{z}, \tilde{\mathbf{x}}(\mathbf{v})) = \tilde{\mathbf{h}}(\mathbf{z}, \mathbf{v}),$$

with $\tilde{\mathbf{x}}(\mathbf{v}) = [\mathbf{q}^n + \delta t \mathbf{N}^n \mathbf{v}, \mathbf{v}]$. Then we linearize the external system dynamics around \mathbf{z}^n and \mathbf{v}^n to obtain

$$\begin{aligned}\dot{\mathbf{z}}(\mathbf{z}, \mathbf{v}) &\approx \partial_z \tilde{\mathbf{h}}^n \mathbf{z} + \partial_v \tilde{\mathbf{h}}^n \mathbf{v} + \mathbf{b}_h^n, \\ \mathbf{b}_h^n &= \tilde{\mathbf{h}}(\mathbf{z}^n, \mathbf{v}^n) - \partial_z \tilde{\mathbf{h}}^n \mathbf{z}^n - \partial_v \tilde{\mathbf{h}}^n \mathbf{v}^n.\end{aligned} \quad (26)$$

As in a Rosenbrock integration scheme [15, §IV.7], we integrate the linearized dynamics implicitly as

$$\mathbf{z}^{n+1} = \mathbf{z}^n + \delta t \left(\partial_z \tilde{\mathbf{h}}^n \mathbf{z}^{n+1} + \partial_v \tilde{\mathbf{h}}^n \mathbf{v}^{n+1} + \mathbf{b}_h^n \right). \quad (27)$$

Note that for linear external systems, such as PID controllers, the linearization (26) is exact and the Rosenbrock approximation reduces to implicit Euler.

Remark 2. *In cases where the external system dynamics are sufficiently simple, we can also consider an explicit Euler scheme, which results from replacing (26) with $\dot{\mathbf{z}} = \tilde{\mathbf{h}}(\mathbf{z}^n, \mathbf{v}^n)$. This eliminates the cost of computing $\partial_z \tilde{\mathbf{h}}^n$ and $\partial_v \tilde{\mathbf{h}}^n$, but may force error control to take smaller steps if the external system dynamics (9a) are stiff.*

We solve \mathbf{z}^{n+1} as a function of \mathbf{v}^{n+1} from (27)

$$\mathbf{z}^{n+1} = \mathbf{Z} \mathbf{v}^{n+1} + \mathbf{b}, \quad (28)$$

with

$$\begin{aligned}\mathbf{Z} &= \delta t \left(\mathbf{I} - \delta t \partial_z \tilde{\mathbf{h}}^n \right)^{-1} \partial_v \tilde{\mathbf{h}}^n, \\ \mathbf{b} &= \left(\mathbf{I} - \delta t \partial_z \tilde{\mathbf{h}}^n \right)^{-1} (\mathbf{z}^n + \delta t \mathbf{b}_h^n).\end{aligned}$$

Similarly, we now use (12) and (28) to eliminate \mathbf{q} and \mathbf{z} from the actuation (9b) to produce

$$\boldsymbol{\tau}^{n+1} \approx \mathbf{g}(\mathbf{Z}\mathbf{v}^{n+1} + \mathbf{b}, \tilde{\mathbf{x}}(\mathbf{v}^{n+1})) = \tilde{\mathbf{g}}(\mathbf{v}^{n+1}),$$

and linearize around \mathbf{v}^n to obtain the approximation

$$\boldsymbol{\tau}^{n+1} = \partial_v \tilde{\mathbf{g}}^n(\mathbf{v}^{n+1} - \mathbf{v}^n) + \tilde{\mathbf{g}}^n.$$

To obtain a linear control law compatible with (19), we make one final approximation

$$\boldsymbol{\tau}^{n+1} = -\mathbf{C}\mathbf{v}^{n+1} + \mathbf{d}, \quad (29)$$

with

$$\mathbf{C} = \max(0, \text{diag}(-\partial_v \tilde{\mathbf{g}}^n)), \quad \mathbf{d} = \tilde{\mathbf{g}}(\mathbf{v}^n) + \mathbf{C}\mathbf{v}^n.$$

For stabilizing diagonal linear external systems, including PID controllers, $\mathbf{C} = -\partial_v \tilde{\mathbf{g}}^n$ and we recover an implicit Euler scheme. Moreover, we can also handle (highly non-linear) effort limits using the convex potential (20). In practice, most well-designed control systems are stabilizing. Thus, for non-linear control strategies such as *inverse dynamics PID* or *task space control*, \mathbf{C} is a good approximation of $-\partial_v \tilde{\mathbf{g}}^n$ that greatly improves simulation stability. In the rare case of stiff but non-stabilizing external forces where $\mathbf{C} = \mathbf{0}$, (29) resolves to the explicit approximation $\boldsymbol{\tau}^{n+1} \approx \boldsymbol{\tau}^n$, and error control will shrink the time step accordingly to resolve the dynamics at the requested accuracy.

We compute $\partial_v \tilde{\mathbf{g}}^n$ with forward differences, though more sophisticated alternatives like automatic differentiation are also possible. Finally, with \mathbf{v}^{n+1} computed from the convex ICF, we advance the external state \mathbf{z}^{n+1} using (28).

D. Static and Dynamic Friction

Mathematically, it is impossible for discrete formulations to disambiguate between static and dynamic friction. Ad-hoc extensions to PGS-style solvers from computer graphics [52] are sometimes applied to robotics [3], [4], but without mathematical grounding these methods lack convergence guarantees and can produce hard-to-quantify artifacts.

In contrast, continuous-time formulations offer a rigorous framework for capturing both static and dynamic friction through regularized friction. In particular, we use the model (7), which captures both regimes. However, the negative slope between μ_s and μ_d breaks the convexity of ICF.

To incorporate the non-convex friction model (7) into our convex formulation, we *lag* the regularized term $\mu(s)$ as

$$\mathbf{f}_t^{n+1} = -\mu(\|\mathbf{v}_t^n\|/v_s) \frac{\mathbf{v}_t^{n+1}}{\sqrt{\|\mathbf{v}_t^{n+1}\|^2 + v_s^2}} \mathbf{f}_n^n.$$

This approximation is convex, converges to the continuous model (7) as time step goes to zero (i.e. it is *consistent*), and maintains a tight approximation in stiction (when $\|\mathbf{v}_t^{n+1}\| < v_s$). CENIC keeps the local truncation error introduced by this approximation within the user-requested accuracy by modulating the time step as needed.

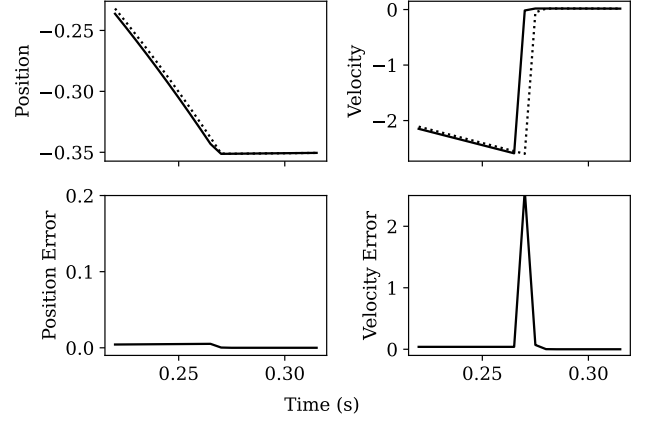


Fig. 4: Vertical position and velocity of a ball dropped on a table, showing differences between solutions computed with a 1 ms (solid line) and a 5 ms (dashed line) time step. Velocity error spikes, but position error does not.

E. The Error Norm

When components of the state \mathbf{x} differ in scale or units, the error estimate can become dominated by certain terms while others are negligible. This is common in multibody systems, where $\mathbf{x} = [\mathbf{q}; \mathbf{v}]$ includes both positions and velocities.

As an example, consider a ball dropped onto a table. Figure 4 shows vertical position, velocity, and corresponding errors for two simulations with different (fixed) time steps. While the trajectories are similar overall, the velocity error exhibits a sharp spike at impact due to the impulsive nature of contact. Even with compliant contact, such rapid velocity changes dominate the error estimate, forcing the integrator to take small steps to capture fast time scales.

To address this issue, we measure error using a weighted position-only L^∞ norm

$$e^{n+1} = \|\mathbf{S}(\mathbf{q}^{n+1} - \hat{\mathbf{q}}^{n+1})\|_\infty,$$

where the diagonal scaling matrix \mathbf{S} maps each component to a dimensionless unit. This makes ε_{acc} in (4) an acceptable fraction of unit error, or equivalently, the desired *digits of accuracy* in the solution [22] (0.1 roughly corresponding to 10%). \mathbf{S} can be estimated from knowledge of coordinate types or it can be specified by expert users.

By excluding impulsive velocity jumps, this norm focuses the error estimate on positions—capturing artifacts such as rattling and passthrough evident in \mathbf{q} . As shown in Section VII-B, this choice reduces simulation times by over an order of magnitude in contact-rich problems.

F. Method Summary

Algorithm 1 summarizes CENIC. Users provide initial conditions, desired accuracy ε_{acc} , and a maximum time step size δt_{max} .

At each step, CENIC linearizes external system dynamics (9) around the current state $(\mathbf{x}^n, \mathbf{z}^n)$. This is used by `DoStep()` to compute the solution \mathbf{x}^{n+1} and error reference $\hat{\mathbf{x}}^{n+1}$. `DoStep()` uses either the first-order step-doubling method (Section V-A) or the second-order trapezoid method

Algorithm 1: CENIC

Input: $\mathbf{x}^0, \mathbf{z}^0, \varepsilon_{\text{acc}}, \delta t_{\text{max}}, T$
 $t \leftarrow 0$
 $n \leftarrow 0$
 $\delta t \leftarrow k_{\text{init}} \delta t_{\text{max}}$
while $t \leq T$ **do**
 Linearize external systems: (Sec. V-C)
 $\mathbf{Z}, \mathbf{b}, \mathbf{C}, \mathbf{d} = \text{LinearizeExtSys}(\mathbf{x}^n, \mathbf{z}^n)$
 Perform convex optimization: (Sec. V-A-V-B)
 $\mathbf{x}^{n+1}, \hat{\mathbf{x}}^{n+1} = \text{DoStep}(\mathbf{x}^n; \delta t, \mathbf{C}, \mathbf{d})$
 Advance external systems state:
 $\mathbf{z}^{n+1} = \mathbf{Z}\mathbf{v}^{n+1} + \mathbf{b}$
 Estimate the error: (Sec. V-E)
 $e^{n+1} = \|\mathbf{S}(\mathbf{q}^{n+1} - \hat{\mathbf{q}}^{n+1})\|_{\infty}$
 if $e^{n+1} \leq \varepsilon_{\text{acc}}$ **then**
 Accept step and propagate solution:
 $t \leftarrow t + \delta t$
 $\mathbf{x}^n \leftarrow \mathbf{x}^{n+1}$
 $\mathbf{z}^n \leftarrow \mathbf{z}^{n+1}$
 $n \leftarrow n + 1$
 Update the time step:
 $\delta t \leftarrow \text{AdjustStepSize}(\delta t; e^{n+1}, \varepsilon_{\text{acc}})$

(Section V-B). If the error estimate (Section V-E) is below the desired accuracy, the solution is propagated and time is advanced forward.

In practice, `AdjustStepSize()` uses standard step-selection logic [15, §4.8], implementing a dead-band function to introduce hysteresis and prevent repeated step size switches. More precisely

$$\hat{\delta t} = \text{Deadband}(k_{\text{Safe}} \delta t (\varepsilon_{\text{acc}} / e^{n+1})^{1/p}, \delta t),$$

$$\delta t \leftarrow \min(\hat{\delta t}, k_{\text{MaxGrow}} \delta t, \delta t_{\text{max}}),$$

where

$$\text{Deadband}(\delta t_{\text{new}}, \delta t) = \begin{cases} \delta t & \text{if } k_{\text{Low}} \delta t < \delta t < k_{\text{High}} \delta t, \\ \delta t_{\text{new}} & \text{Otherwise.} \end{cases}$$

A mature implementation must also include other safety checks for corner cases such as divide-by-zero or not-a-number (NaN) errors. We use $k_{\text{init}} = 0.1$, $k_{\text{Safe}} = 0.9$, $k_{\text{Low}} = 0.9$, $k_{\text{High}} = 1.2$ and $k_{\text{MaxGrow}} = 5.0$.

VI. PERFORMANCE OPTIMIZATIONS

In this section, we introduce several performance optimizations enabled by error-controlled integration. At each step, CENIC solves a series of convex problems of the form

$$\mathbf{v}^{n+1} = \min_{\mathbf{v}} \ell(\mathbf{v}), \quad (30a)$$

$$\ell(\mathbf{v}) = \frac{1}{2} \mathbf{v}^T \mathbf{A} \mathbf{v} - \mathbf{r}^T \mathbf{v} + \ell_c(\mathbf{v}). \quad (30b)$$

We solve each convex problem iteratively with Newton's method. At the i -th iteration, the Newton update is

$$\mathbf{H}_i \mathbf{p}_i = -\mathbf{g}_i \quad (31a)$$

$$\mathbf{v}_{i+1} = \mathbf{v}_i + \alpha_i \mathbf{p}_i, \quad (31b)$$

where $\mathbf{H}_i = \nabla^2 \ell(\mathbf{v}_i)$ is the Hessian, $\mathbf{g}_i = \nabla \ell(\mathbf{v}_i)$ the gradient, \mathbf{p}_i the search direction, and α_i is computed with exact linesearch [16]. The optimizations described below aim to solve this sequence of problems more efficiently.

A. Warm Starts

Primal formulations like (30) are easily warm started from prior solutions. For the step-doubling scheme (Section V-A), we warm start the full step to $\hat{\mathbf{v}}^{n+1}$ with \mathbf{v}^n , the first half-step to $\mathbf{v}^{n+1/2}$ with $(\mathbf{v}^n + \hat{\mathbf{v}}^{n+1})/2$, and the second half-step to \mathbf{v}^{n+1} with $\hat{\mathbf{v}}^{n+1}$. For the trapezoid scheme (Section V-B), we warm start the first order solution $\hat{\mathbf{v}}^{n+1}$ with \mathbf{v}^n , and the second order solution \mathbf{v}^{n+1} with $\hat{\mathbf{v}}^{n+1}$.

B. Adaptive Convergence Criteria

Robotics simulations typically require tight convergence to ensure stable contacts [2], [16]. With error control, however, Newton iterations (31) only need to converge to a tolerance that is negligible compared to the requested accuracy [15].

CENIC uses two convergence criteria. The first checks the optimality condition

$$\|\mathbf{D}\mathbf{g}\| \leq \epsilon_{\text{tol}} \max(1, \|\mathbf{D}\mathbf{r}\|), \quad (32)$$

where $\mathbf{D} = \text{diag}(\mathbf{M})^{-1/2}$ scales all variables to have the same units [16] and ϵ_{tol} is a dimensionless tolerance. This criterion allows for early exit even before any Newton iterations take place, in case the initial guess is a solution within the required tolerance.

The second criterion evaluates the convergence of Newton iterations to the true solution \mathbf{v}^* . Following [15, p. 121], the true error $\|\mathbf{v}^* - \mathbf{v}_{i+1}\|$ is estimated from the norm of $\Delta \mathbf{v}_i = \mathbf{v}_{i+1} - \mathbf{v}_i$. This leads to the criterion

$$\eta_i \|\mathbf{D}^{-1} \Delta \mathbf{v}_i\| \leq \epsilon_{\text{tol}} \max(1, \|\mathbf{D}\mathbf{r}\|), \quad (33)$$

where \mathbf{D}^{-1} scales velocities to the same units as (32), and

$$\Theta_i = \|\Delta \mathbf{v}_{i+1}\| / \|\Delta \mathbf{v}_i\|,$$

$$\eta_i = \Theta_i / (1 - \Theta_i).$$

In fixed-step mode, we use a tight tolerance $\epsilon_{\text{tol}} = 10^{-8}$ suitable for stable discrete-time simulation. In error controlled mode, we instead set

$$\epsilon_{\text{tol}} = \max(\kappa \cdot \varepsilon_{\text{acc}}, 10^{-8}), \quad (34)$$

for some $\kappa \in [0, 1]$. We found $\kappa = 0.001$ to provide a reasonable balance between performance and stable contact resolution across all of our test cases.

C. Hessian Reuse

Since consecutive convex solves differ only slightly, we reuse factorizations in analogy to Jacobian reuse in implicit Runge–Kutta methods [15, §IV.8]. Unlike implicit Runge–Kutta, however, CENIC does not require monitoring Newton's method for divergence, as ICF's convexity [17] guarantees convergence for any positive definite Hessian approximation, albeit possibly slowly for poor approximations.

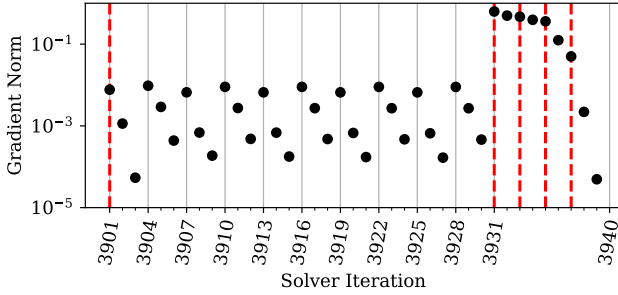


Fig. 5: Solver convergence during hard clutter simulation, illustrating the impact of Hessian reuse. Red dashed lines indicate a recomputed Hessian, while light grey lines separate time steps. (35) allows us to reuse the same Hessian when possible (first ten steps). When necessary, a few fresh factorizations enable rapid Newton-type convergence (final step).

Instead, we estimate the convergence error after a desired maximum number of iterations N . If this satisfies criterion (33), we can keep reusing the current Hessian approximation. Otherwise, the Hessian is recomputed. The actual number of iterations can be higher, N is simply a *desired* maximum.

Assuming linear convergence rate Θ_i (conservative for Newton), the true error $\|\mathbf{v}^* - \mathbf{v}_{i+M}\|$ after M additional iterations is $\Theta_i^M / (1 - \Theta_i) \|\Delta \mathbf{v}_i\|$. Thus we recompute the Hessian if

$$\frac{\Theta_i^{N-i}}{1 - \Theta_i} \|\Delta \mathbf{v}_i\| \geq \epsilon_{tol} \max(1, \|\mathbf{D}\mathbf{r}\|), \quad (35)$$

where $N = 10$ in our implementation. Using this criterion, we reuse Hessians not only across iterations, but also across convex solves and time steps.

Figure 5 shows the convergence history of a test simulation from Sec. VII, illustrating the effectiveness of the approach. Reusing the same factorization across time steps yields fast but only linear convergence; when this reuse becomes limiting, the method detects it, recomputes the Hessian, and recovers quadratic convergence.

D. Cubic Linesearch Initialization

Our exact linesearch uses Newton-Raphson with bisection fallback [53, §9.4]. Although the required first and second derivatives can be evaluated in linear time [16, §IV.C], linesearch remains a significant cost (Sec. VII-F).

A better initial guess can reduce this cost. In [16], [17], the initial guess is from a quadratic approximation of $\ell_\alpha(\alpha) := \ell(\mathbf{v} + \alpha p)$ using $\ell_\alpha(0)$, $\ell'_\alpha(0)$, and $\ell''_\alpha(0)$. In this work, we instead use a cubic approximation, constructed from $\ell_\alpha(0)$, $\ell'_\alpha(0)$, $\ell_\alpha(\alpha_{\max})$, and $\ell'_\alpha(\alpha_{\max})$. Typically $\alpha_{\max} = 1$, though values as large as $\alpha_{\max} = 1.5$ also work well.

VII. EXPERIMENTAL RESULTS

This section presents simulation results characterizing the performance of CENIC. Throughout this section, we refer to five test cases shown in Fig. 6. These scenarios highlight different challenges in robotics simulation.

First, a **cylinder** falls onto a table (Fig. 6a). While this example is simple, the cylinder’s sharp corners produce

forces that vary abruptly with changes in state. The cylinder has radius 0.1 m, length 0.2 m, and mass 6.3 kg.

The next case isolates grasping complexity to its simplest form—a peg wedged between two stationary fingers of a **static gripper** (Fig. 6b). The gripper slides along a prismatic joint and impacts the ground; the peg should remain wedged through this impulsive event. Despite the apparent simplicity of this scenario, many methods exhibit unstable friction oscillations, as shown in Fig. 7. The peg is a $1 \times 1 \times 8$ cm block. Each finger is a $1 \times 1 \times 8$ cm block spaced such that the gap between them is 0.01 mm narrower than the peg’s width. The fingers are rigidly attached to a $4 \times 4 \times 20$ cm post. All bodies have the density of water.

The **Franka** example (Fig. 6c) reflects a typical robotics workflow. A high-gain inverse-dynamics controller drives a Franka Emika Panda arm between two setpoints while the gripper grasps a Cheez-It® box. Beyond testing force closure between the gripper and box, this case also requires simulating a stiff user-defined controller. As discussed in Section V-C, the high controller gains introduce short time scales that challenge numerical stability.

The **soft clutter** and **hard clutter** examples test scalability by dropping 20 objects into a bin. The soft clutter case uses only spheres, a contact stiffness of 10^3 N/m, and a large friction regularization ($v_s = 1$ cm/s). The hard clutter case mixes spheres and cubes, with stiffer contact parameters approximating rigid Coulomb friction: contact stiffness 10^5 N/m and stiction tolerance 0.1 mm/s.

The first three examples (cylinder, gripper, franka) use hydroelastic contact [23], [24], while both clutter examples use point contact. All tests were completed on the same workstation with an Intel Xeon w7-3565X CPU.

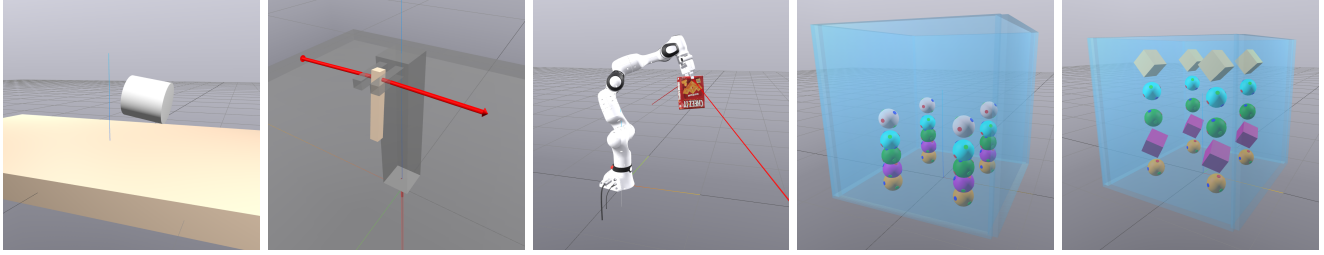
A. Comparing First and Second-Order Methods

As shown in Fig. 8, the second-order method improves energy conservation through contact, where a 1 kg ball with zero dissipation is dropped from an initial height of 1 m. The energy conservation error decays quadratically with δt under the trapezoid method, but only linearly with step-doubling.

But this benefit is offset by a loss of stability, which forces the trapezoid method to take much smaller time steps to control stability rather than accuracy. As shown in Fig. 9, the second-order trapezoid method is consistently 5-20 times slower than step-doubling on the hard clutter example, despite requiring fewer convex solves per time step. For this reason, and because strict energy conservation is rarely a critical requirement for robotics simulation, we **prefer the first-order step-doubling** approach and use it for the remainder of this paper.

B. Comparison with Other Error-Controlled Integrators

We compare CENIC with several state-of-the-art error-control baselines. Our first baseline is implicit euler (**IE**) with step-doubling for error estimation, a first-order L -stable scheme. We use a mature implementation with Jacobian reuse and accuracy-driven stopping criteria [15, §IV.8]. We



(a) **Cylinder** falls on a table. (b) **Static gripper** holds a peg. (c) **Franka Panda** moves a box. (d) **Soft clutter** falls in a box. (e) **Hard clutter** falls in a box.

Fig. 6: Simulation test cases, ranging from least to most complex. These test cases highlight different challenges in robotics simulation: sharp corners (a), stable force closure (b), stiff nonlinear controllers (c), many degrees-of-freedom (d), and complex contact interactions (e).

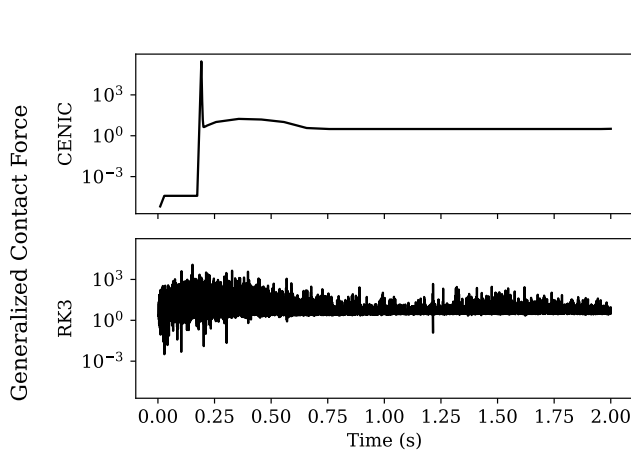


Fig. 7: Contact force magnitude for the static gripper example at accuracy $\varepsilon_{\text{acc}} = 10^{-3}$. CENIC (top) produces smooth, stable contact forces, while RK3 (bottom) produces noisy, unstable results. Deceivingly, positions might look visually accurate with RK3, until later in the simulation when RK3 mistakenly drops the object.

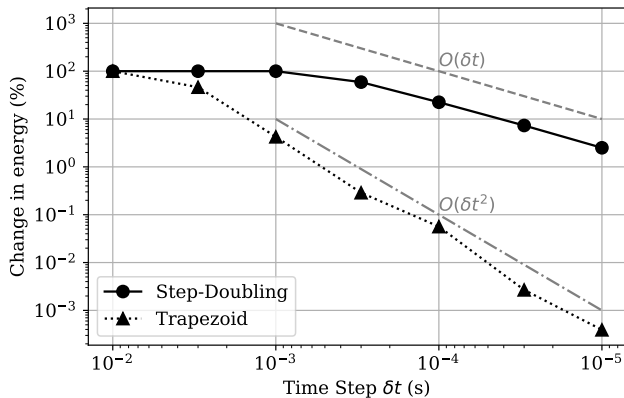


Fig. 8: Energy conservation error (percent of energy lost after 10 seconds) for a 0.1 kg bouncing ball with zero dissipation. The ball is relatively soft (contact stiffness 10^3 N/m) and bounces 11 times in the 10 second simulation. Potential energy is defined such that total energy is zero when the ball is at rest on the ground. The trapezoid method (Sec. V-B) shows second-order convergence, while step-doubling (Sec. V-A) is first order.

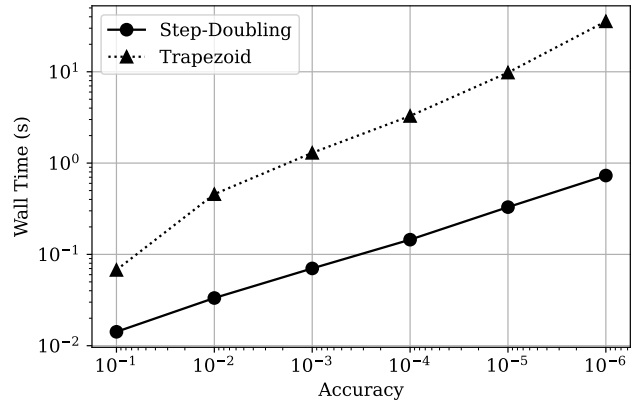


Fig. 9: Work-precision plots for hard clutter (lower is better). Despite requiring only two convex solves per step versus three for step-doubling, the trapezoid method’s lack of stability hinders performance.

also compare with a third-order Runge-Kutta scheme (**RK3**). Unlike IE, RK3 is an explicit scheme, and is not L -stable.

For higher order L -stable baselines, we compare with the **SDIRK2** method [54] and the two-stage Rosenbrock method **ROS2** [55], both second-order. Rosenbrock methods are essentially implicit Runge-Kutta methods that only take one Newton iteration per step [15]. Rosenbrock methods are known to be particularly effective on stiff problems at loose accuracies. Our implementation is based on [56].

Figure 10 shows work-precision plots comparing these four baselines with CENIC. All implementations are in C++ using Drake [6]. Since our baseline integrators implement only dense algebra, for a fair comparison we report CENIC results with both sparse and dense Cholesky factorizations. In addition to comparing integration schemes across examples, Fig. 10 also illustrates the impact of computing an error estimate over the full state (top) and over positions only (bottom), as discussed in Section V-E.

While the baseline integration schemes produce acceptable results for the simpler examples (e.g., cylinder, gripper), only CENIC is able to simulate the hard clutter scenario faster than real time. Additionally, considering position error enables a consistent order-of-magnitude speedup for CENIC, but not for the other baselines. This is likely due to the tightly converged frictional contact solution produced by ICF in a single step, while other integrators must take many small time

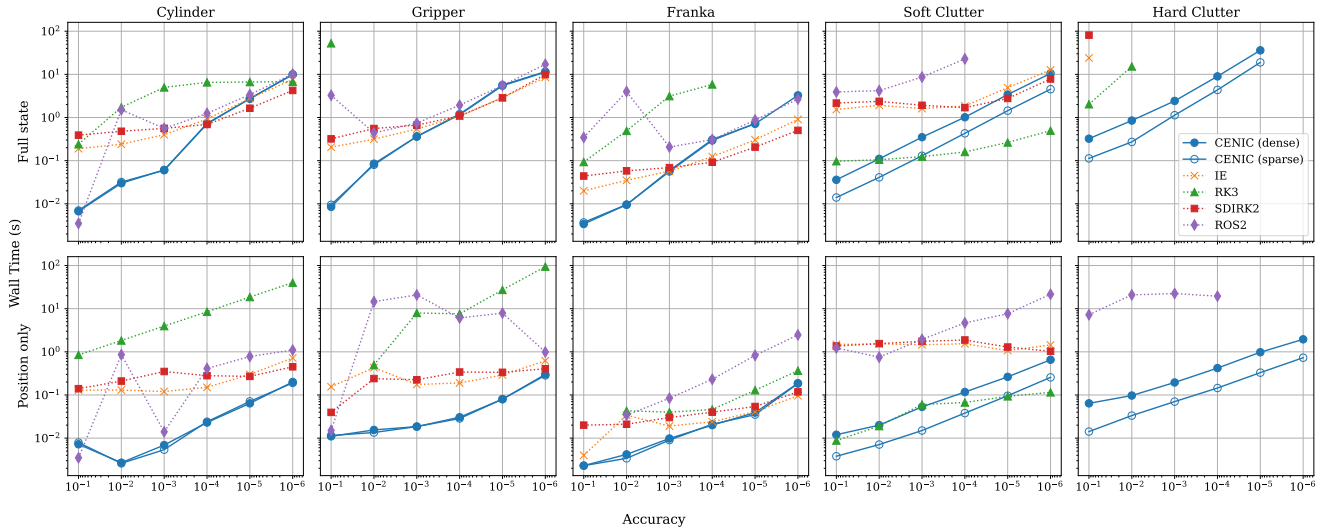


Fig. 10: Work-precision plots for the test cases in Fig. 6, using error control on the full state \mathbf{x} (top) and on positions \mathbf{q} only (bottom). Lower is better. Wall times are normalized to one second of simulation time. Missing data points indicate solver failure or timeout after 100 seconds (real-time rate < 1%). CENIC performs particularly well with many contacts and at loose accuracies, where convergence failures force other implicit schemes to take small steps.

steps to maintain stability and resolve stick-slip transitions. Moreover, ICF requires a single geometric query per convex solve, while standard integrators need to update geometric quantities at every Newton iteration.

C. Comparison with Discrete-Time Robotics Simulators

We compare simulation speeds with two test cases shown in Fig. 11: three large mesh bunnies (height 1 m, mass 200 kg) and an unactuated Boston Dynamics Spot model, both dropped on the ground. The Spot model is from the MuJoCo Menagerie [57], while the bunny model is from the Stanford 3D Scanning Repository [58]. The bunnies are simulated for 10 seconds (at which point they cease rolling), while the quadruped is simulated for 3 seconds.

We compare CENIC against discrete solvers in MuJoCo [2], IsaacSim [3], Genesis [5], and Drake [6]. Except for the time step, we use default simulator parameters. Figure 11 shows wall times for all simulators using 1 ms and 10 ms fixed time steps, as well as for CENIC with accuracies $\varepsilon_{\text{acc}} \in [10^{-1}, 10^{-3}, 10^{-5}]$. Remarkably, CENIC achieves comparable simulation speeds, even though it is tasked to compute a solution to desired accuracy.

This test evaluates speed only, not quality. All simulators produced visually plausible results, though their differing parameterizations and stiffness choices lead to distinct trade-offs between speed and physical realism. For example, when simulating the Spot model with a 1 ms time step, MuJoCo required 7613 solver iterations but allowed up to 3.1 cm of ground penetration, whereas CENIC (in fixed-step mode) required 9056 iterations but produced only 6.4 mm of penetration. A full analysis of these trade-offs and their implications for sim-to-real transfer is an important area for future work, but outside the scope of this paper.

D. Novel Capabilities

We highlight several capabilities of CENIC that are difficult, or even mathematically impossible, to incorporate into existing discrete-time simulators.

1) *Stiff External Systems*: As discussed in Section V-C, CENIC integrates external systems implicitly. This allows for modular design: users can define arbitrarily complex systems, including those with internal state, without modifying or recompiling the solver or any multibody component. In contrast, popular robotics simulators offer limited support for modeling controllers (often only PD control), while complex user-defined subsystems must be handled explicitly, leading to unstable coupling with the multibody dynamics.

As a first example, the Franka arm in Fig. 6c tracks desired positions \mathbf{q}_d and velocities \mathbf{v}_d using an inverse dynamics controller

$$\begin{aligned} \boldsymbol{\tau} &= \mathbf{M}(\mathbf{q})\dot{\mathbf{v}}_d + \mathbf{k}(\mathbf{q}, \mathbf{v}), \\ \dot{\mathbf{v}}_d &= -K_p(\mathbf{q} - \mathbf{q}_d) - K_d(\mathbf{v} - \mathbf{v}_d), \end{aligned}$$

where K_p and K_d are proportional and derivative gains, respectively. Figure 12 contrasts an explicit treatment of this nonlinear external system (as done in most simulators) with our proposed diagonally-implicit approach. Our scheme allows CENIC to handle extremely high gains without the need to take more time steps—step size is solely determined by the requested accuracy, not stability.

This modular capability extends beyond controller modeling. Figure 13 illustrates a vacuum gripper composed of an array of bellows, each modeled as a small-mass cylinder attached to a spring-loaded prismatic joint. Suction from each bellow is modeled as a force on nearby objects inversely proportional to distance. Bellows are pressed against the pad as objects are caught by the vacuum. The combination of light masses and strong suction forces makes this system particularly challenging for standard discrete-time approaches.

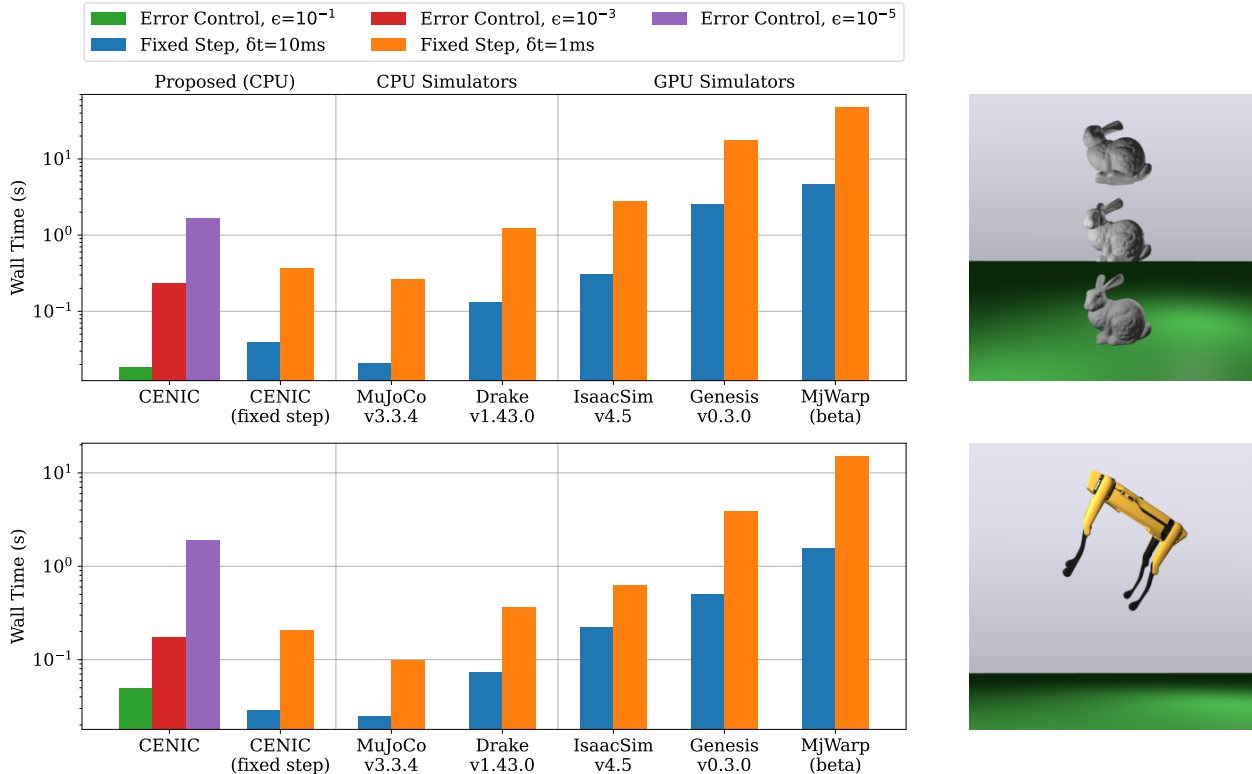


Fig. 11: Simulator speed comparison. Three mesh bunnies (top) and an unactuated quadruped robot (bottom) are dropped on the ground. CENIC is competitive with state-of-the-art robotics simulators in both fixed-step and error-controlled mode. Note that these benchmarks measure speed only, not simulation quality. Also note that the GPU simulators are optimized for simulating many parallel scenes, but these tests use only a single scene.

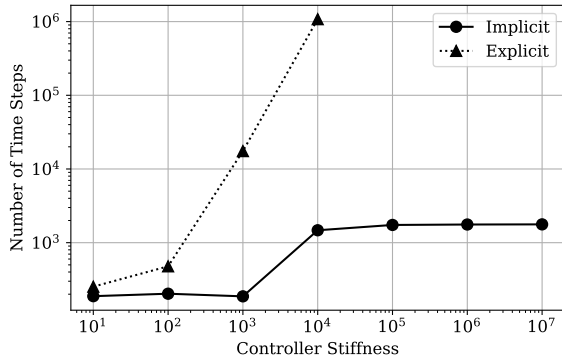


Fig. 12: Number of time steps required to simulate the franka task for 10 seconds with different controller stiffnesses ($= K_p = K_d$) and accuracy $\epsilon_{\text{acc}} = 0.01$. With a standard explicit treatment, step size must decrease to keep stability under control. In contrast, our proposed implicit scheme (Sec. V-C) is stable even with extremely stiff controllers.

With discrete time-stepping, large forces treated explicitly lead to severe passthrough (Fig. 13b). In contrast, CENIC advances the solution without artifacts (Fig. 13c).

2) *Static and Dynamic Friction*: CENIC provides, for the first time, a mathematically rigorous treatment of distinct static and dynamic friction coefficients that is compatible with the high speed and scalability requirements of robotics simulation (Section V-D).

To demonstrate this, we simulate a 1 kg block sitting on

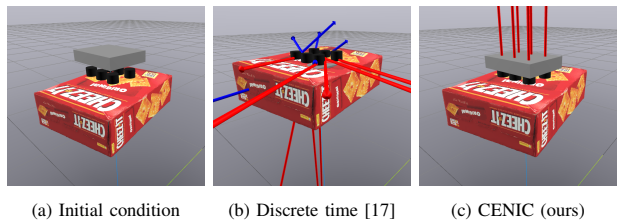


Fig. 13: Suction gripper after 0.5s of simulation. For discrete time-stepping, we use $\delta t = 0.01$ s. For CENIC, we request accuracy $\epsilon_{\text{acc}} = 10^{-3}$. Large forces pulling the box into the gripper lead to massive passthrough artifacts in the discrete-time simulation. CENIC resolves the dynamics correctly with a combination of error control (Section V-A) and implicit treatment of the gripper force model (Section V-C).

an oscillating conveyor belt. Friction coefficients between belt and box are $\mu_s = 1.0$ and $\mu_d = 0.5$. Figure 14 plots tangential friction force and velocity relative to the conveyor belt. The box transitions between stiction and sliding, with contact force jumps due to distinct friction coefficients. As accuracy is tightened, impulsive transitions from sliding back to stiction become evident.

E. Hardware Validation

To evaluate CENIC in a practical manipulation scenario, we consider a real-to-sim task involving numerous challenging objects (Fig. 1), inspired by the most demanding benchmarks used to assess large behavior model (LBM) performance in simulation [59]. In this **dish rack** scenario, a

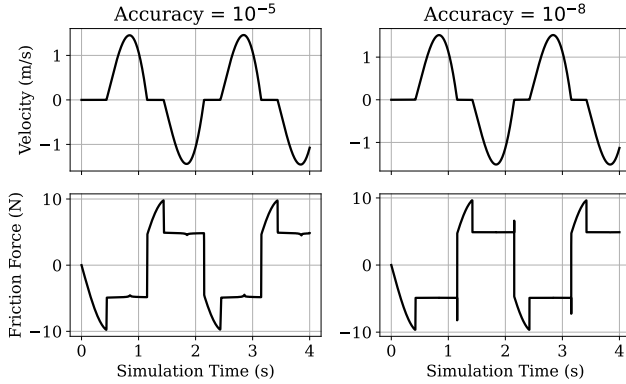


Fig. 14: Tangential velocities and friction forces for a 1 kg box on an oscillating conveyor belt, demonstrating transitions between static ($\mu_s = 1.0$) and dynamic ($\mu_d = 0.5$) friction. An accuracy of 10^{-5} (left) shows the box “catching” in stiction at low velocities. A tight accuracy (10^{-8} , right) is needed to capture the impulsive transition from sliding to stiction. Existing convex time-stepping methods are unable to capture any of these effects, as they only support a single coefficient of friction.

Accuracy	10^{-1}	10^{-2}	10^{-3}	10^{-4}
Real-time rate	218%	463%	342%	132%
Artifacts	Yes (15d)	Yes (15e)	No	No
Time Step (s)	0.02	0.01	0.002	0.001
Real-time rate	102%	180%	43%	21%
Artifacts	Yes (15a)	Yes (15b)	Yes (15c)	No

TABLE I: Performance comparison between error-controlled integration (top) and fixed-step integration (bottom) on the dishrack simulation (Fig. 1). Error-controlled integration eliminates obvious artifacts (shown in Fig. 15) while achieving faster overall simulation speeds.

teleoperated robot drops several thin objects into a plastic bin, then dumps the contents of the bin on a wire dish rack. We then replay the recorded trajectories in simulation, tracking joint angles with a high-gain PD controller. We use hydroelastic contact with high moduli (10^8 Pa) to model hard objects. Thin, complex collision geometries, varying masses, high elastic moduli, heavy robot arms, and stiff controller gains make this scenario particularly challenging.

Discrete time-stepping struggles with major artifacts on this task, as shown in Fig. 15. Thin objects interacting with the bin and the wire dishrack make the simulation vulnerable to passthrough and rattling, despite the use of a sophisticated hydroelastic contact model [23], [24]. As shown in Table I, we need to reduce the time step to 1 ms to eliminate all visually-obvious artifacts. With this small time step, the simulation runs much slower than real time.

In contrast, error-controlled CENIC eliminates all visually-obvious artifacts at an accuracy of $\epsilon_{\text{acc}} = 10^{-3}$, while completing the simulation faster than real time (342% real-time rate). Screenshots comparing the simulation and real-world trajectories are shown in Fig. 16. While the trajectories do not match exactly (unsurprising given chaotic dynamics and open-loop playback), the results are qualitatively similar and obvious discretization artifacts are absent. Moreover, contact forces are smooth, leading to robust grasping.

With error control, the real-time rate varies throughout the simulation, as shown in Fig. 17. During complex collisions, such as when the robot dumps objects onto the wire rack

Accuracy	10^{-1}	10^{-2}	10^{-3}	10^{-4}	10^{-5}
Wall time (adaptive)	0.19	0.39	0.65	1.11	2.69
Wall time (fixed)	0.21	0.41	0.71	1.19	2.69
Iterations (adaptive)	4015	9973	19235	39537	95839
Iterations (fixed)	4591	10938	20865	40729	95839

TABLE II: Impact of adaptive convergence criteria (Sec VI-B) on hard clutter simulation times (in seconds) and total solver iterations.

Error control	Reuse	Wall time (s)	Steps	Facts.	Iters.
Off	Off	0.26	1000	3980	3980
Off	On	0.27	1000	2293	6068
On	Off	0.65	499	16624	16624
On	On	0.61	510	10557	19235

TABLE III: Impact of Hessian reuse on the hard clutter example. Hessian reuse reduces the number of expensive factorizations (“Facts.”), at the cost of more iterations. With error control enabled ($\epsilon_{\text{acc}} = 10^{-3}$, maximum timestep 0.1 s), this offers a small improvement in overall performance. In fixed step mode ($\delta t = 10$ ms), Hessian reuse does not improve performance.

around 70–80 s, the time step decreases, reducing the real-time rate. As the objects settle, the simulator takes larger steps. **This adaptive stepping enables faster overall simulation despite the added cost of error estimation.**

F. Performance Profiling

In this section, we characterize the computational cost breakdown of CENIC, with particular attention to the impact of the performance optimizations described in Section VI.

Figure 18 shows the computational cost of major components for our five main examples (Fig. 6) as well as the dish rack demonstration (Fig. 16), all at accuracy $\epsilon_{\text{acc}} = 10^{-3}$. The breakdown varies considerably between problems, with no single component always dominating. Geometry queries are often a major component, particularly for scenarios with hydroelastic contact (cylinder, gripper, franka, dish rack).

Table II compares performance with and without the adaptive convergence criterion from Sec. VI-B. The adaptive criterion, which uses looser tolerances under looser accuracies, enables mild speedups. While a larger κ can produce faster solve times, we found that a more conservative $\kappa = 10^{-3}$ provides a good balance between speed and stable resolution of contact forces.

Table III characterizes the impact of Hessian reuse (Sec. VI-C) on the hard clutter example. While similar Jacobian reuse strategies are essential for obtaining good performance in implicit Runge-Kutta schemes [15], we find that Hessian reuse provides only a modest benefit with error control enabled, and no improvement in fixed-step mode.

Figure 19 quantifies the impact of cubic linesearch initialization (Sec. VI-D). Note that as accuracy is tightened, fewer linesearch iterations are required, since the optimization problem is easier to solve for small time steps. Cubic linesearch initialization offers a small but consistent reduction in the total number of linesearch iterations relative to a fixed-guess strategy ($\alpha_0 = 1.0$) and the quadratic initialization strategy implemented in [16].

VIII. DISCUSSION AND LIMITATIONS

CENIC is the first error-controlled integrator specialized for robotics, outperforms existing error-controlled integrators



(a) Fixed step, $\delta t = 0.02$ s (b) Fixed step, $\delta t = 0.01$ s (c) Fixed step, $\delta t = 0.002$ s (d) Error control, $\epsilon_{\text{acc}} = 10^{-1}$ (e) Error control, $\epsilon_{\text{acc}} = 10^{-2}$

Fig. 15: Undesirable artifacts from simulating the dish rack example (Fig. 1) with a too-large time step (fixed-step mode) or a too-loose accuracy (error control mode). Tightening the accuracy is a more efficient means of eliminating these artifacts than reducing the time step, as shown in Table I

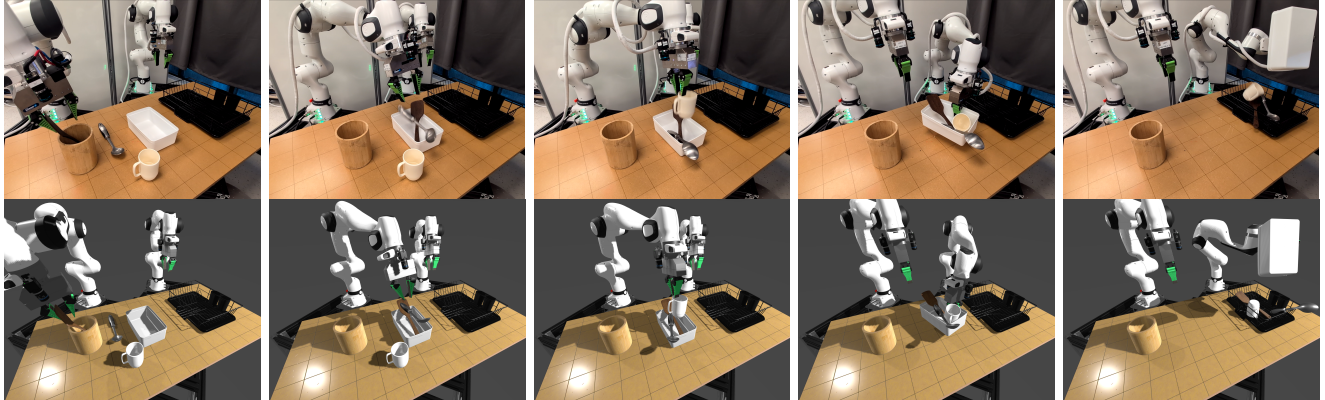


Fig. 16: Snapshots of the dish rack task on hardware (top) and in simulation with CENIC (bottom, $\epsilon_{\text{acc}} = 10^{-3}$). The simulation and real trajectories are not exactly the same, due to model sensitivity and chaotic dynamics. But the overall qualitative behavior in simulation matches the real-world demonstration: there are no drops, missed grasps, passthrough incidents, rattling, or other major numerical artifacts. In contrast, standard discrete time-stepping methods introduce major artifacts, even with relatively small time steps (Fig. 15a-c).

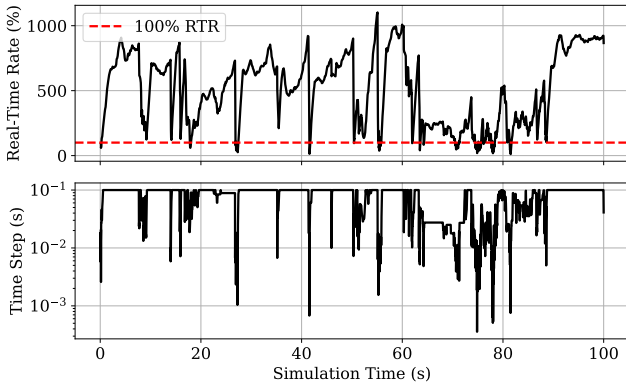


Fig. 17: Real-time rate and step size δt for the complex dishrack simulation (Fig. 1) at accuracy $\epsilon_{\text{acc}} = 10^{-3}$. By only taking small time steps when needed to resolve stiff collision dynamics, CENIC achieves faster overall simulation times than discrete time-stepping (Table I).

by orders of magnitude, and runs at speeds comparable to state-of-the-art discrete-time simulators.

Error control yields inherent robustness: users can focus on modeling their controllers and external systems, while CENIC automatically adapts the time step to ensure accuracy and stabilize stiff dynamics that would otherwise become unstable under standard discrete schemes. With CENIC, users specify a desired accuracy rather than a time step, eliminating a common pain point in authoring multibody simulations.

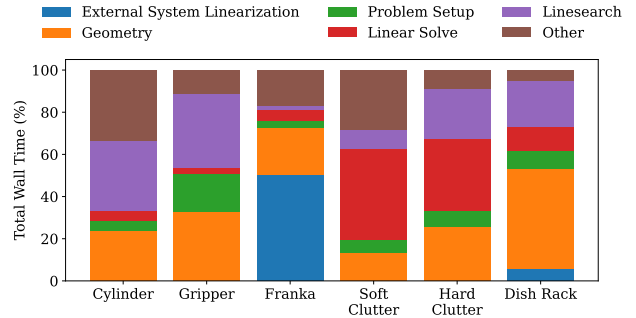


Fig. 18: Computational cost breakdown for each of the examples, run with error control at accuracy $\epsilon_{\text{acc}} = 10^{-3}$.

Moreover, by controlling accuracy, CENIC separates the numerical truncation error introduced by the time-stepping scheme from modeling error arising from simplifying mathematical assumptions, inaccurate parameters, or user mistakes.

CENIC incorporates engineering-grade, experimentally validated contact models and, for the first time, provides a formal framework with mathematical guarantees for modeling dry friction using distinct static and dynamic coefficients while meeting the high speed requirements of robotics simulation. This stands in contrast to common game-engine approaches, where PGS-style solvers handle friction iteratively through ad-hoc clipping heuristics, which lack convergence

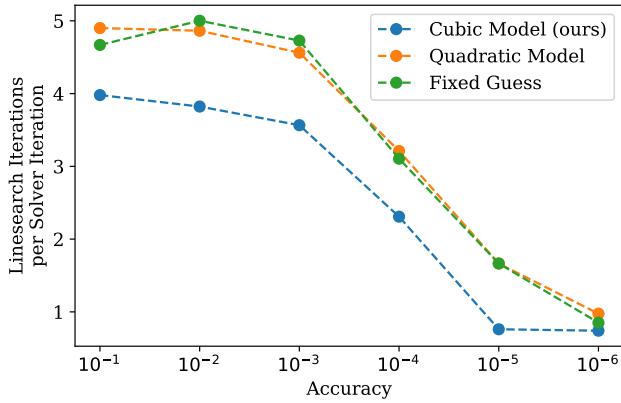


Fig. 19: Comparing different strategies for choosing an initial guess for linesearch, for the hard clutter problem at different accuracies. Our cubic spline method consistently reduces the number of iterations required for exact linesearch, resulting in modest improvements in overall speed.

and accuracy guarantees and can produce artifacts or difficult-to-diagnose instabilities.

Thanks to its basis in convex ICF, CENIC guarantees convergence at each time step. At the same time, CENIC maintains consistency: numerical artifacts vanish as accuracy is tightened, recovering the true trajectory of a given model.

For interactive simulation, we find that CENIC is most effective at loose accuracy settings around $\varepsilon_{\text{acc}} = 10^{-3}$, which is sufficient to eliminate major discretization artifacts in dexterous manipulation scenarios. Since step-doubling is first order, it is less efficient at tight tolerances, where higher-order schemes may offer better performance, an interesting avenue for future research. Notably, we observed that instability in a second-order trapezoidal method severely degraded performance compared to first-order step-doubling.

CENIC is most effective in offline simulation, where over long horizons it surpasses fixed-step integration by taking larger steps during slow dynamics while maintaining accuracy and robustness. Real-time fluctuations currently limit its use in interactive teleoperation, though we expect this to improve with CPU and GPU parallelization (all results so far used a single CPU thread).

We believe that fast error-controlled robotics simulation will open the door to better sim-to-real transfer, model identification, and policy learning, and more. Future work will focus on verifying the usefulness of CENIC in these applications, with a particular focus on systematic hardware validation of sim-to-real transfer.

IX. CONCLUSION

We presented CENIC, a new method for simulating multi-body dynamics with contact that combines modern convex time-stepping with traditional error-controlled integration. CENIC eliminates discretization artifacts, outperforms existing error-controlled integrators by orders of magnitude, and achieves simulation speeds on par with state-of-the-art discrete-time robotics simulators. Additionally, CENIC can integrate arbitrary user-defined controllers implicitly and

rigorously simulate dry friction with different static and dynamic coefficients, all while maintaining guaranteed accuracy and convergence.

Most importantly, CENIC disentangles numerical discretization error from modeling error while maintaining the fast simulation speeds required by modern robotics workflows. We hope that this will enable accelerated progress in sim-to-real transfer, model identification, policy learning and evaluation, and model-based control for robotics.

REFERENCES

- [1] E. Coumans and Y. Bai, “Pybullet, a python module for physics simulation for games, robotics and machine learning,” <http://pybullet.org>, 2016–2020.
- [2] E. Todorov, T. Erez, and Y. Tassa, “Mujoco: A physics engine for model-based control,” in *2012 IEEE/RSJ international conference on intelligent robots and systems*. IEEE, 2012, pp. 5026–5033.
- [3] NVIDIA, “Nvidia physx,” 2020. [Online]. Available: <https://developer.nvidia.com/physx-sdk>
- [4] J. Hwangbo, J. Lee, and M. Hutter, “Per-contact iteration method for solving contact dynamics,” *IEEE Robotics and Automation Letters*, vol. 3, no. 2, pp. 895–902, 2018. [Online]. Available: www.raim.com
- [5] G. Authors, “Genesis: A universal and generative physics engine for robotics and beyond,” December 2024. [Online]. Available: <https://github.com/Genesis-Embodied-AI/Genesis>
- [6] R. Tedrake and the Drake Development Team, “Drake: Model-based design and verification for robotics,” 2019. [Online]. Available: <https://drake.mit.edu>
- [7] P. J. Roache, *Verification and validation in computational science and engineering*. Hermosa Albuquerque, NM, 1998, vol. 895.
- [8] W. L. Oberkampf and C. J. Roy, *Verification and validation in scientific computing*. Cambridge university press, 2010.
- [9] Hexagon, “Adams.” [Online]. Available: <https://hexagon.com/products/product-groups/computer-aided-engineering-software/adams>
- [10] Siemens, “Simcenter 3D.” [Online]. Available: <https://plm.sw.siemens.com/en-US/simcenter/simulation-test/motion-simulation/>
- [11] EnginSoft, “RecurDyn.” [Online]. Available: <https://enginsoftusa.com/RecurDynMBD/Flexible-Multibody-Dynamics-with-Recurdyn.html>
- [12] L. W. Nagel, “Spice2: A computer program to simulate semiconductor circuits,” *College of Engineering, University of California, Berkeley*, 1975.
- [13] K. L. Johnson and K. L. Johnson, *Contact mechanics*. Cambridge university press, 1987.
- [14] K. H. Hunt and F. R. E. Crossley, “Coefficient of restitution interpreted as damping in vibroimpact,” 1975.
- [15] E. Hairer and G. Wanner, *Solving ordinary differential equations II*. Springer Berlin Heidelberg New York, 1996, vol. 375.
- [16] A. M. Castro, F. N. Permenter, and X. Han, “An unconstrained convex formulation of compliant contact,” *IEEE Transactions on Robotics*, vol. 39, no. 2, pp. 1301–1320, 2022.
- [17] A. Castro, X. Han, and J. Masterjohn, “Irrotational contact fields,” *arXiv preprint arXiv:2312.03908*, 2024.
- [18] H. Hertz, “The contact of elastic solids,” *J Reine Angew. Math*, vol. 92, pp. 156–171, 1881.
- [19] Y. Gonthier, *Contact dynamics modelling for robotic task simulation*. University of Waterloo West Waterloo, ON, Canada, 2007.
- [20] L. Luo and M. Nahon, “A compliant contact model including interference geometry for polyhedral objects,” 2006.
- [21] G. Hippmann, “An algorithm for compliant contact between complexly shaped bodies,” *Multibody System Dynamics*, vol. 12, no. 4, pp. 345–362, 2004.
- [22] M. A. Sherman, A. Seth, and S. L. Delp, “Simbody: multibody dynamics for biomedical research,” *Procedia Iutam*, vol. 2, pp. 241–261, 2011.
- [23] R. Elandt, E. Drumwright, M. Sherman, and A. Ruina, “A pressure field model for fast, robust approximation of net contact force and moment between nominally rigid objects,” in *2019 IEEE/RSJ International Conference on Intelligent Robots and Systems (IROS)*. IEEE, 2019, pp. 8238–8245.
- [24] J. Masterjohn, D. Guoy, J. Shepherd, and A. Castro, “Velocity level approximation of pressure field contact patches,” *IEEE Robotics and Automation Letters*, vol. 7, no. 4, pp. 11 593–11 600, 2022.

- [25] M. Schuderer, G. Rill, T. Schaeffer, and C. Schulz, "Friction modeling from a practical point of view," *Multibody System Dynamics*, vol. 63, no. 1, pp. 141–158, 2025.
- [26] J. R. Dormand and P. J. Prince, "A family of embedded runge-kutta formulae," *Journal of computational and applied mathematics*, vol. 6, no. 1, pp. 19–26, 1980.
- [27] Dassault Systemes, "Simpack." [Online]. Available: <https://www.3ds.com/products/simulia/simpack>
- [28] —, "MotionSolve." [Online]. Available: <https://altair.com/motionsolve>
- [29] T. Geijtenbeek, "The Hyfydy simulation software," 11 2021, <https://hyfydy.com>. [Online]. Available: <https://hyfydy.com>
- [30] F. Pfeiffer and C. Glocker, *Multibody Dynamics with Unilateral Contacts*, ser. Wiley Series in Nonlinear Science. Wiley, 1996.
- [31] J.-S. Pang and D. E. Stewart, "Differential variational inequalities," *Mathematical programming*, vol. 113, no. 2, pp. 345–424, 2008.
- [32] D. E. Stewart and J. C. Trinkle, "An implicit time-stepping scheme for rigid body dynamics with inelastic collisions and coulomb friction," *International Journal for Numerical Methods in Engineering*, vol. 39, no. 15, pp. 2673–2691, 1996.
- [33] M. Anitescu and F. A. Potra, "Formulating dynamic multi-rigid-body contact problems with friction as solvable linear complementarity problems," *Nonlinear Dynamics*, vol. 14, no. 3, pp. 231–247, 1997.
- [34] D. M. Kaufman, S. Sueda, D. L. James, and D. K. Pai, "Staggered projections for frictional contact in multibody systems," *ACM Trans. Graph.*, vol. 27, no. 5, Dec. 2008.
- [35] D. E. Stewart, "Convergence of a time-stepping scheme for rigid-body dynamics and resolution of painlevé's problem," *Archive for Rational Mechanics and Analysis*, vol. 145, no. 3, pp. 215–260, 1998.
- [36] K. Erleben, "Velocity-based shock propagation for multibody dynamics animation," *ACM Transactions on Graphics (TOG)*, vol. 26, no. 2, pp. 12–es, 2007.
- [37] M. Li, Z. Ferguson, T. Schneider, T. R. Langlois, D. Zorin, D. Panozzo, C. Jiang, and D. M. Kaufman, "Incremental potential contact: intersection- and inversion-free, large-deformation dynamics," *ACM Trans. Graph.*, vol. 39, no. 4, p. 49, 2020.
- [38] M. Macklin, K. Erleben, M. Müller, N. Chentanez, S. Jeschke, and V. Makoviychuk, "Non-smooth newton methods for deformable multi-body dynamics," *ACM Transactions on Graphics (TOG)*, vol. 38, no. 5, pp. 1–20, 2019.
- [39] T. A. Howell, S. Le Cleac'h, J. Z. Kolter, M. Schwager, and Z. Manchester, "Dojo: A differentiable simulator for robotics," *arXiv preprint arXiv:2203.00806*, vol. 9, no. 2, p. 4, 2022.
- [40] J. Carpentier, L. Montaut, and Q. L. Lidec, "From compliant to rigid contact simulation: a unified and efficient approach," *arXiv preprint arXiv:2405.17020*, 2024.
- [41] "AGX Dynamics," <https://www.algoryx.se/products/agx-dynamics>.
- [42] CM Labs Simulations, "Theory guide: Vortex software's multibody dynamics engine," <https://www.cm-labs.com/vortexstudiodocumentation>.
- [43] R. Smith, "Open dynamics engine," 2004. [Online]. Available: <https://www.ode.org>
- [44] M. Anitescu, "Optimization-based simulation of nonsmooth rigid multibody dynamics," *Mathematical Programming*, vol. 105, no. 1, pp. 113–143, 2006.
- [45] E. Todorov, "Convex and analytically-invertible dynamics with contacts and constraints: Theory and implementation in mujoco," in *2014 IEEE International Conference on Robotics and Automation (ICRA)*. IEEE, 2014, pp. 6054–6061.
- [46] D. Kang and J. Hwangho, "SimBenchmark. Physics engine benchmark for robotics applications: RaiSim vs. Bullet vs. ODE vs. MuJoCo vs. DartSim." <https://leggedrobotics.github.io/SimBenchmark>.
- [47] H. Mazhar, T. Heyn, A. Pazouki, D. Melanz, A. Seidl, A. Bartholomew, A. Tasora, and D. Negrut, "Chrono: a parallel multi-physics library for rigid-body, flexible-body, and fluid dynamics," *Mechanical Sciences*, vol. 4, no. 1, pp. 49–64, 2013.
- [48] V. Acary and F. Péron, "Siconos: A software platform for modeling, simulation, analysis and control of nonsmooth dynamical systems," *SNE Simulation News Europe*, vol. 17, no. 3/4, pp. 19–26, 2007.
- [49] Q. Le Lidec, W. Jallet, L. Montaut, I. Laptev, C. Schmid, and J. Carpentier, "Contact models in robotics: a comparative analysis," *IEEE Transactions on Robotics*, 2024.
- [50] M. Software, "Adams 2021.0.2 adams solver user's guide," 2021. [Online]. Available: https://help-be.hexagonmi.com/bundle/Adams_2021.0.2_Adams_Solver_User_Guide/raw/resource/enus/Adams_2021.0.2_Adams_Solver_User_Guide.pdf
- [51] U. M. Ascher, S. J. Ruuth, and B. T. Wetton, "Implicit-explicit methods for time-dependent partial differential equations," *SIAM Journal on Numerical Analysis*, vol. 32, no. 3, pp. 797–823, 1995.
- [52] M. Müller, M. Macklin, N. Chentanez, S. Jeschke, and T.-Y. Kim, "Detailed rigid body simulation with extended position based dynamics," in *Computer Graphics Forum*, vol. 39, no. 8. Wiley Online Library, 2020, pp. 101–112.
- [53] W. H. Press, S. A. Teukolsky, W. T. Vetterling, and B. P. Flannery, "Numerical recipes 3rd edition," *Cambridge: New York*, 2007.
- [54] C. A. Kennedy and M. H. Carpenter, "Diagonally implicit runge-kutta methods for ordinary differential equations. a review," Tech. Rep., 2016.
- [55] D. S. Blom, P. Birken, H. Bijl, F. Kessels, A. Meister, and A. H. van Zuijlen, "A comparison of rosenbrock and esdirk methods combined with iterative solvers for unsteady compressible flows," *Advances in Computational Mathematics*, vol. 42, pp. 1401–1426, 2016.
- [56] H. Zhang and A. Sandu, "Fatode: A library for forward, adjoint, and tangent linear integration of odes," *SIAM Journal on Scientific Computing*, vol. 36, no. 5, pp. C504–C523, 2014.
- [57] K. Zakka, Y. Tassa, and MuJoCo Menagerie Contributors, "MuJoCo Menagerie: A collection of high-quality simulation models for MuJoCo," 2022. [Online]. Available: http://github.com/google-deepmind/mujoco_menagerie
- [58] S. U. C. G. Laboratory, "The stanford 3d scanning repository," 1994. [Online]. Available: <https://graphics.stanford.edu/data/3Dscanrep/>
- [59] J. Barreiros, A. Beaulieu, A. Bhat, R. Cory, E. Cousineau, H. Dai, C.-H. Fang, K. Hashimoto, M. Z. Irshad, M. Itkina *et al.*, "A careful examination of large behavior models for multitask dexterous manipulation," *arXiv preprint arXiv:2507.05331*, 2025.